Comparison between Suspension Plasma Sprayed (SPS) and High Velocity Suspension Flame Sprayed (HVSFS) bioactive coatings

Giovanni Bolelli, Devis Bellucci, Valeria Cannillo, Rainer Gadow, Andreas Killinger, Luca Lusvarghi, Philipp Müller, Antonella Sola

PII: S0257-8972(15)30213-9
DOI: doi: 10.1016/j.surfcoat.2015.08.039
Reference: SCT 20513

To appear in: *Surface & Coatings Technology*

Received date: 29 May 2015
Revised date: 31 July 2015
Accepted date: 20 August 2015

Please cite this article as: Giovanni Bolelli, Devis Bellucci, Valeria Cannillo, Rainer Gadow, Andreas Killinger, Luca Lusvarghi, Philipp Müller, Antonella Sola, Comparison between Suspension Plasma Sprayed (SPS) and High Velocity Suspension Flame Sprayed (HVSFS) bioactive coatings, *Surface & Coatings Technology* (2015), doi: 10.1016/j.surfcoat.2015.08.039

Comparison between Suspension Plasma Sprayed (SPS) and High Velocity Suspension Flame Sprayed (HVSFS) bioactive coatings

Giovanni Bolelli[1,*], Devis Bellucci[1], Valeria Cannillo[1], Rainer Gadow[2], Andreas Killinger[2], Luca Lusvarghi[1], Philipp Müller[2], Antonella Sola[1]

[1] Department of Engineering "Enzo Ferrari", University of Modena and Reggio Emilia, Via P. Vivarelli 10/1, I-41125 Modena, Italy.

[2] Institute for Manufacturing Technologies of Ceramic Components and Composites (IMTCCC), Universität Stuttgart, Allmandring 7b, D-70569 Stuttgart, Germany

* Corresponding author. Tel.: 0039 0592056233; Fax: 0039 0592056243;
e-mail: giovanni.bolelli@unimore.it

Abstract

This paper assesses the diverse potentialities of two different suspension spraying processes, namely High Velocity Suspension Flame Spraying (HVSFS) and Suspension Plasma Spraying (SPS), for the deposition of bioactive coatings based on hydroxyapatite and on a new, custom-made K_2O-Na_2O-CaO-P_2O_5-SiO_2 bioactive glass.

With both feedstock types, the HVSFS process imparts high in-flight velocities to the particles and aggregates released after solvent vaporisation, resulting in well flattened, tightly bound lamellae. The coatings, <50 μm thick and very dense, have hardness and elastic modulus values close to those of the corresponding bulk materials. They can be employed as high-quality bioactive layers on metallic implantable devices. Few days of soaking in simulated body fluid (SBF) results in the re-precipitation of a surface hydroxyapatite layer, albeit through different mechanisms. In HVSFS bioactive glass coatings, ion leaching turns the surface into a silica gel, onto which hydroxyapatite subsequently deposits. In HVSFS hydroxyapatite, the amorphous fraction is progressively dissolved and microcrystalline hydroxyapatite precipitates onto the remaining coating layer.

The SPS technique, due to the lower in-flight velocity of particles and agglomerates, always produces more porous, rougher layers with columnar-like growth. They are not mechanically strong, but their peculiar structure can be useful for specific, functional applications. The high surface area of porous SPS bioactive glass coatings favours ion leaching and fast dissolution in simulated body fluid (SBF); hence, it is suggested that SPS bioglass could be useful as a rapidly resorbable layer. SPS hydroxyapatite, by contrast, is more stable than the corresponding HVSFS layer, despite its porosity, because of the higher crystallinity. After the amorphous fraction is dissolved in SBF, newly formed hydroxyapatite does not constitute a surface layer but precipitates inside the pores, suggesting that a sealing pre-treatment in SBF could be a means to tune porosity and phase composition.

Keywords

Suspension thermal spray; bioactive coating; bioactive glass; hydroxyapatite; simulated body fluid (SBF) test; microstructure

1. Introduction

Titanium and its alloys are extensively used as biomaterials for orthopaedic and dental applications (i.e. joint and hip replacements, pins, screws for fracture fixation, bone plates, etc.) due their biocompatibility, excellent corrosion resistance, lower density than other metallic biomaterials and suitable mechanical properties [1-4]. However, these materials do not form a chemical bond with bone after implantation, and the human body encapsulates them in a fibrous capsule to isolate them from the surrounding tissue. In order to promote osseointegration, the surface of titanium and its alloys is often coated with hydroxyapatite (HA), a calcium phosphate ceramic that is similar to the mineral phase of bone [5-8]. Although several methods are currently available to produce HA coatings, such as sputtering, electrophoretic deposition, sol-gel processing, pulsed laser deposition, etc. [9-15], the only commercially accepted technique is the conventional atmospheric plasma spray process. It consists of injecting a dry powder feedstock into a thermal plasma jet, which heats the particles and accelerates them towards the substrate, where they impact, flatten and get deposited in the form of lamellae (also called "splats") [8,9,16,17]. In spite of its high productivity, relatively low cost and moderate heat input conveyed to the substrate, this process has a series of drawbacks, including possible chemical and structural alterations of crystalline bioactive ceramics (such as HA) and the inability to deposit thin (<50 μm thick) coatings [18]. In particular, as the processing temperature increases, HA can be decomposed to tricalcium-phosphate and to tetracalcium-phosphate; the formation of CaO can also be observed as a result of thermal degradation [18-21]. On the other hand, the need for thin coatings is emerging in the field of bioactive ceramics as a large thickness is not only superfluous in order to impart osseoconductive or even osseoinductive properties to the coated surfaces, but it is also detrimental to adhesion and long-term mechanical stability [22]. A high thickness is indeed likely to induce relevant deposition stresses, which undermine the adhesion and may cause long-term de-bonding between the coating and the substrate,

resulting in the implant failure and/or in the release of undesirable debris in the surrounding tissues [18,23].

The innovative suspension thermal spray techniques [24-26] are ideally suited to deposit thin layers and, on the other hand, they share the common fundamental advantages of all thermal spray processes. Namely, in comparison to alternative deposition techniques, they feature high productivity and relatively low processing cost, including the fact that the coatings do not need any post-deposition heat treatment for consolidation, as it occurs e.g. in the case of electrophoretic coatings of pure HA [27-29]. Since in the suspension thermal spray process the feedstock is dispersed in a liquid medium, which ensures good flowability, the particle size distribution of the powder can be much finer than in conventional atmospheric plasma spraying, resulting in thinner lamellae. Both in conventional thermal spraying and in suspension thermal spraying, the coating consists of the superposition of a certain number of lamellae, but in the latter case, since the splat thickness is much lower, the minimum thickness limit for the coating is reduced; hence, deposits of less than 50 μm can be obtained.

More specifically, two of the available suspension thermal spray processes, High-Velocity Suspension Flame Spraying (HVSFS) and suspension plasma spraying (SPS), have already shown their potential for the manufacturing of bioactive coatings.

The High-Velocity Suspension Flame Spraying (HVSFS) [30-32] technique employs a modified gas-fuelled high velocity oxygen-fuel (HVOF) torch in order to process the liquid suspension. As the latter is axially injected inside the combustion chamber of the torch, complete mixing of the suspension drops with the gas is favoured. The solid particles (released after solvent vaporisation) are heated by the gas in the combustion chamber and in the expansion nozzle and, as the gas stream attains supersonic velocity upon expansion to ambient pressure outside the torch, they are also dragged to extremely high velocities (up to 900 m/s according to some recent estimates [33,34]). Extensive flattening onto the substrate is achieved, resulting in very dense layers with high cohesive / adhesive strength, which has already been experimentally verified both for calcium-phosphate

coatings (tricalcium phosphate [34] and hydroxyapatite [31]) and for bioactive glass coatings [35]. The latter, even though somewhat prone to crystallise at high temperature, offer several advantages with respect to HA [36-39], since they do not decompose during thermal spraying and they possess a higher bioactivity index than HA. Among bioactive glasses, 45S5 Bioglass®, first proposed by Prof. Hench at the end of the 1960s [6], is the most bioactive one and it is able to bond both to bone and to soft tissues. Recently the ability of 45S5 Bioglass® to induce neovascularisation and to promote stem cells differentiation into osteoblasts has also been stated [40,41].

The suspension plasma spraying (SPS) process injects the liquid suspension into a thermal plasma jet, issuing out of a standard atmospheric plasma spraying torch [24,25,42]. Due to the radial injection scheme, and to the periodic fluctuations in plasma energy, liquid drops follow very different trajectories in the gas stream [42-44]. The particles therefore reach the substrate with a wide range of temperatures and velocities. In an attempt to overcome this issue, recent research has investigated the design of "resonant-mode" torches where a "drop-on-demand" injector is synchronised with a plasma operating with regular, periodic pulsations [45,46]. However, such devices are not yet available on the market; hence, most research is still carried out using "standard" atmospheric plasma torches.

Moreover, under typical thermal plasma conditions, the gas mean free path of ~0.4 μm (according to [47]) is comparable to the size of micrometric or sub-micrometric particles. This gives rise to non-continuum effects, also known as Knudsen effect, which drastically decrease the heat and momentum transfer from the gas to the particles [47-49]. This issue does not affect the HVSFS process, because the high-pressure and low-temperature gas (compared to a thermal plasma) possesses lower mean free path [47]. Considering that the plasma is also strongly cooled by the suspension solvent evaporation, the result is that particles are poorly heated and are accelerated to much lower velocities than with the HVSFS process. SPS coatings are therefore typically more porous and rougher than HVSFS ones. Their microstructure is further modified by the extremely large heat flux which a thermal plasma jet delivers at the short stand-off distances (often comprised

in the 30 – 60 mm range) used in the SPS process. Quantitative calorimetric measurements have indeed returned values from 2-8 MW/m^2 [50] up to maxima of 20 MW/m^2 [47,51,52], 25 MW/m^2 [53] or even 37 MW/m^2 [54], compared to values of <1 MW/m^2 for conventional atmospheric plasma spraying at stand-off distances of ≈100 mm [50,53]. Such heat fluxes are likely to induce sintering of the deposited material, which was shown in [52,55] and numerically demonstrated in [56], based on the solid-state diffusion theory.

The microstructures of SPS ceramics therefore frequently exhibit peculiar features, such as the co-existence of flattened lamellae together with regions made up of sintered, unmelted particles [55,57,58]. The porosity of these coatings also differs considerably from that of conventional atmospheric plasma sprayed ones. Whilst the latter contains larger, micrometric pores and elongated inter- and intra-lamellar microcracks, SPS coatings typically contain numerous, rounded, sub-micrometric pores [59]. The distribution of all microstructural features in SPS coatings is further sensitive to the properties of the suspension (average particle size, dispersion, etc.) [57,58].

On the other hand, the SPS technique is highly versatile and flexible and, differently from the HVSFS process, there is no risk to build up crusts of material on the inside of the torch, which is a known source of defects in the coating due to the periodic ejection of fragments of the crust [60]. Due to such flexibility, the SPS technique has already been proposed for a large variety of functional applications, including the manufacturing of gas-sensing layers [61], of solid oxide fuel cells [62], and of thermal barrier coatings [63]. The latter example also shows an instance where porous SPS coatings prove to be advantageous over denser HVSFS ones, because of better compliance (resulting in enhanced thermal shock resistance) and lower thermal conductivity.

Several authors have also considered the use of SPS for the deposition of bioactive glass coatings of various compositions, with promising *in vitro* responses from simulated body fluid (SBF) soaking tests [64-67].

In the present contribution, these two different suspension thermal spray systems, namely the HVSFS and SPS processes, were therefore comparatively studied. Two different material systems were chosen: a commercially available HA nanopowder and a new custom-made bioactive glass powder (hereafter referred to as "BG-Ca/Mix"), which is employed here for the first time as feedstock for suspension thermal spraying. The BG-Ca/Mix has been recently obtained from the reference 45S5 Bioglass® by increasing its CaO content and by replacing part of Na_2O with K_2O [68,69]. This new glass, which has been tested for the production of glass-matrix/calcium phosphate composites and of enamelled coatings [70,71], has indeed shown very promising properties, including a low tendency to crystallise compared to 45S5 Bioglass® and a high *in vitro* bioactivity in SBF [72].

2. Materials and Methods

2.1 Preparation of powders and suspensions

As previously mentioned, two different raw materials were employed: a commercially available nano-sized HA powder (average particle size ≈ 100 nm) dispersed in diethylene glycol (10 wt.%), provided by Ce.Ri.Col. S.p.A. (Sovigliana, Vinci, FI), and a BG-Ca/Mix powder (glass composition in oxide mol%: 2.3 K_2O, 2.3 Na_2O, 45.6 CaO, 2.6 P_2O_5 and 47.3 SiO_2) [68,69]. The latter was obtained by melting analytical grade raw materials (K_2CO_3, Na_2CO_3, $CaCO_3$, $Ca_3(PO_4)_2$, SiO_2, by Carlo Erba Reagenti, Italy) in Pt crucibles at 1450 °C for 1 h, casting into water ("fritting") and dry milling in porcelain jars using Al_2O_3 balls. The resulting powders were sieved below 38 μm and subsequently attrition milled in isopropanol. The attrition mill was loaded with 600 g of 6 mm-diameter ZrO_2 milling balls, 200 g of sieved glass powder and 80 g of isopropanol. At the end of the attrition milling process, the powder was reduced down to an average particle size of ≈2 μm. The

powder was then dispersed in a 60 wt.% water + 40 wt.% isopropanol mixture, to obtain a suspension with 20 wt.% solid.

2.2 Coating deposition

Four different parameter sets were employed for the SPS deposition of both the BG-Ca/Mix suspension and the HA suspension, as summarized in Table 1. The SPS process was performed using a F6 atmospheric plasma torch (GTV GmbH, Luckenbach, Germany) equipped with a 6 mm-diameter anode nozzle. Based on preliminary experiments, two different injector types were employed for the BG-Ca/Mix and HA suspensions. For the former, the standard F6 anode nozzle was modified to obtain a seating for an internal injector with an orifice of 0.3 mm diameter, delivering a continuous stream of suspension at an injection angle of 90° with respect to the nozzle axis. The HA suspension, on the other hand, was fed through an external injector with the same diameter, providing a continuous stream at an angle of 75°. In both cases, the suspension was fed to the injector through a volumetric pump system.

The HVSFS system has already been described in [30-36]. It consists of a modified gas-fuelled HVOF torch (Top Gun-G, GTV GmbH) equipped with a cylindrical combustion chamber and a liquid injection nozzle (ending up with a 0.9 mm diameter orifice) replacing the standard dry powder feeding port. A continuous stream of suspension is supplied through the volumetric pump system employed for the SPS process. Five different parameter sets were used for the HVSFS deposition of the BG-Ca/Mix suspension (Table 2). Instead, for the HVSFS deposition of HA, only one set of parameters was considered (Table 2), since it had already been optimised in a previous work [31].

As a term of comparison, a HA coating was also produced by spraying an agglomerated and sintered hydroxyapatite powder of -45+22 μm nominal particle size (Ceram GmbH, Albbruck-Birndorf, Germany) by a conventional atmospheric plasma spraying (APS) process, using the same

F6 plasma torch (GTV GmbH) equipped with a standard 6 mm-diameter nozzle and an external powder injection port. APS process parameters are summarised in Table 3.

All samples were deposited onto grade-2 Ti plates (100 x 100 x 3 mm size), grit-blasted with 260 μm-size corundum particles at a pressure of 6 bar. An intermediate TiO_2 layer (bond coat) was preliminarily applied by atmospheric plasma spraying as described in [31,73], since it was found to significantly enhance the adhesion strength of both bioactive glass coatings and hydroxyapatite ones [31,73].

2.3 Structural and microstructural characterisation

The phase composition of the coatings was assessed by X-ray diffraction (XRD: X'Pert PRO, PANAlytical, Almelo, The Netherlands) using Cu–Kα radiation (wavelength: 1.540598 nm). The diffraction patterns were collected in the 10°–70° 2θ range (step size: 0.02°; scan rate: 5 s⁄step). Further investigations were performed by micro-Raman spectroscopy employing a Jobin-Yvon Raman Microscope spectrometer (Horiba Jobin-Yvon Inc., Edison, NJ) with a 632.8 diode laser. Photons scattered by the samples were collected on a CCD camera. The spectrum collection setting involved 6 acquisitions of 40 s each. The collection optic was set at 100 X ULWD objective.

The coatings' microstructure was observed by scanning electron microscopy (SEM: XL30, FEI Co., Eindhoven, The Netherlands) and environmental scanning electron microscopy (ESEM: Quanta 200, FEI) on polished cross-sections and on fracture surfaces (obtained in liquid nitrogen). The ESEM was operated in low-vacuum mode with a pressure of 0.7 mbar. Qualitative chemical analyses were obtained by X-ray energy dispersive spectroscopy (EDS) (Inca, Oxford Instruments, UK).

The hardness and elastic modulus of the coatings were measured by depth-sensing Berkovich nanoindentation (Nano-indentation tester, Anton-Paar Tritec, Peseux, Switzerland) performed on

polished cross-sections with a load of 100 mN. The results were analysed using the Oliver–Pharr method [74], according to ISO 14577.

2.4. Assessment of in vitro bioactivity

10x10 mm samples were cut from the plates and soaked in SBF, prepared according to the procedure described in [72]. Each sample was immersed in 20 ml of SBF in a sealed plastic flask and kept at 37 °C in a controlled environment chamber (MPM Instruments S.r.l., Bernareggio, MI, Italy). The SBF was refreshed every two days. The samples were removed from the SBF after 1, 3, 7 and 14 days, rinsed in bi-distilled water and dried at room temperature for 24 h. The soaked samples were characterised by XRD, by micro-Raman spectroscopy, and by ESEM (same experimental conditions listed above).

3. Results and Discussion

3.1 Structure and microstructure – Bioactive glass coatings

3.1.1 Microstructure of the SPS bioactive glass coatings

It is clear that the SPS process is particularly well suited to the deposition of rough, porous glass layers of ≤50 μm thickness (Fig. 1), consisting of incompletely flattened particles which are only partly attached to one another. This characteristic, better seen in the fracture sections of Fig. 2, is most likely due to the low inertia of these micron-sized glass particles, coupled to the fact that, as mentioned in the Introduction, many of them do not reach the plasma core and do not attain particularly high in-flight velocities. These slow particles are easily deflected and cooled down by the stagnation flow existing in front of the substrate, so that their eventual temperature and velocity at impact do not allow complete flattening and adhesion between adjacent lamellae.

Specifically, the degree to which the trajectory of a particle entrained in a gas flow is affected by perturbations to the flow streamlines (e.g. turbulent eddies, stagnation flow, etc.) is expressed by the Stokes number. The latter is defined as $St = \tau_A/\tau_F$, i.e. it is the ratio between the characteristic time scale of the aerodynamic response of the particle (τ_A) and the characteristic time scale of the gas flow perturbation (τ_F) [75]. As the Stokes number decreases below unity, particles increasingly tend to copy the flow streamlines. As detailed in [34], the Stokes number for a thermally-sprayed particle facing the stagnation flow can be expressed as (1):

(1)

Where: $\rho_{p,}$ = particle density ≈ 2900 kg/m^3;

d_p = particle diameter;

d = thickness of the stagnation flow ≈ 10 mm [76];

U = gas velocity ≈ 400 m/s [77];

μ_g = gas viscosity ≈ 6*10^{-5} kg/(m·s) [77,78];

For particle diameters d_p = 5 µm / 3 µm / 1 µm it follows St ≈ 2.7 / 1.0 / 0.1 respectively, i.e. particles of 1 µm diameter or less undergo significant deflection before reaching the substrate. This implies that the particles acquire a tangential velocity component (i.e. parallel to the substrate surface), so that they tend to stick preferentially to prominent asperities. This results in the irregular growth of columnar- or cone-shaped features as described in detail in [79], accounting for the rough morphology of the coatings (Fig. 1).

More specifically, two kinds of particles are identifiable, both on fracture sections (Fig. 2(a,b)) and on top surfaces (Fig. 2(c,d)): larger particles containing internal porosity and smaller particles (around or below 1 µm in diameter) containing no internal pores (detail in Fig. 2(b)). The latter come from individual, primary glass particles. The former, by contrast, are obtained when aggregates of primary particles are heated above the glass transition temperature. In this case, indeed, the aggregates sinter in a single, larger droplet containing internal gas porosity, as previously depicted in [34]. As mentioned previously, both kinds of particles reached the substrate

with relatively low velocity and temperature, which prevented complete flattening. Probably, the particles deposited on the substrate and seen in Fig. 2 are only a small portion of the sprayed material, whilst many of the particles (especially of the smallest ones) failed to stick to the underlying surface, as testified by their very low Stokes number.

The BG-Ca/Mix sample deposited under process parameter set #1 differs remarkably from all other SPS glass coatings, because of its much greater thickness and its peculiar structure, which consists of columns of sintered glass (Fig. 3(a), 4(a)) containing spherical bubbles (Fig. 3(b), 4(b)). In greater detail, it is clear that this coating is composed of a thin bottom layer (Fig. 3(c)), probably deposited during the first torch cycles, on top of which these sintered, bubbly columns grow during the final cycles (Fig. 2(d)).

The most likely explanation for this phenomenon resides in the large surface temperatures attained during this deposition (Table 1), as the system is progressively heated up during each of the eight torch cycles. As the surface temperature exceeds the glass transition temperature, the deposition rate increases abruptly because most of the incoming glass particles (even the slowest and coldest ones) can easily stick onto the underlying viscous glass surface. Accordingly, the particles that are still recognisable near the top surface (Fig. 4(c, d)), in spite of their poor flattening degree, show clear evidence of sintering to the surrounding material. As these particles continued being deflected along horizontal trajectories by the stagnation flow, the coating growth mechanism remained mainly columnar.

At the same time, large-scale viscous flow sintering processes above the glass transition temperature gave rise to closed, spherical porosities due to the entrainment of gas bubbles as previously seen in Figs. 3(b), 4(b).

3.1.2 Microstructure of the HVSFS bioactive glass coatings

The BG-Ca/Mix samples deposited by HVSFS (Fig. 5) have a completely different microstructure. They all consist of dense, 20 – 50 μm thick layers containing few rounded pores and some transverse microcracks.

In the HVSFS process, the gas stream and, consequently, the entrained particles travel at much higher velocity than in the suspension plasma spray process. For instance, according to [77], a suspension plasma sprayed particle of 3 μm diameter attains a velocity of 200 – 250 m/s at a stand-off distance of 60 mm, in a free jet condition. This value probably decreases further in the presence of the substrate, due to the stagnation flow as explained in Section 3.1.1. Some literature computations accordingly suggest impact velocities around or well below 100 m/s [80]. In the HVSFS process, by contrast, particles were estimated to reach velocities as high as 900 m/s, with fewer deflection effects [34]. Moreover, suspension injection in the HVSFS process is axial [30-35], so that most of the liquid drops experience maximum heating and acceleration. The resulting molten glass droplets therefore approach the substrate location with sufficiently high velocity in order to overcome the stagnation flow, impinging with a preponderant normal velocity component. This results in extensively flattened lamellae, which achieve excellent cohesion, as seen in the fracture sections of Fig. 6(a, c, e).

These coatings are much denser and more uniform than previous HVSFS-deposited bioactive glass layers, including layers of the standard 45S5 bioglass [35,73]. This could perhaps be ascribed to differences between the thermo-physical properties of these materials (e.g. density, glass transition temperature, viscosity vs. temperature trend, etc.), although a dedicated study would be needed to assess the relation between the characteristics of a glass and its deposition behaviour in the HVSFS process.

In sample #3 (Fig. 6(a)), lamellae are completely sintered together and almost undistinguishable, except for the top surface (Fig. 6(b)), as the system temperature during deposition (Table 2) was the highest. This coating was indeed sprayed with the “hottest” process parameters, namely the highest

propane flow rate and the lowest oxygen flow rate (which implies maximum flame temperature) and minimum stand-off distance (resulting in high heat input to the substrate). In all cases, the lamellae observed on the top surface are much more flattened than those previously seen on the top surface of the SPS samples (compare Figs. 5(b, d, f) to Figs. 2(c, d)). Flattening is particularly good when the spraying distance is lower, as in sample #3 (Fig. 5(b): compare to Figs. 5(d, f)), because this condition maximises the impact velocity of the particles.

The HVSFS samples, however, sometimes exhibit defects due to the presence of large, cracked splats onto their surface (Fig. 7). Visual inspection of the torch, dismounted after the deposition process, indeed revealed some build-up of material along the inner walls of the combustion chamber and of the expansion nozzle. It is likely that, while spraying, some portions of this deposit were, at times, detached and projected towards the substrate, where they formed these large and clearly undesirable defects. The same phenomenon was reported previously [60]. Changing to the most recent version of the HVSFS system, which (as described in [81]) features *ad hoc* modifications to prevent these deposits, would most likely overcome this issue.

It may be stated that the HVSFS process is by far preferable whenever thin, dense, high quality glass layers are required. The hardness and elastic modulus values of these coatings (Table 4), obtained by Berkovich depth-sensing nano-indentation, accordingly resemble those of a bulk glass material [68], although data scatter (witnessed by the related standard deviation values shown as error figures in Table 4) is quite large, due to the presence of some pores and of weaker lamellar boundaries. On the other hand, no significant indentation test could be performed on the SPS samples due to their high porosity.

However the porous, irregular SPS layers could be very useful as rapidly resorbable coatings (due to their higher specific surface area: see Section 3.3) and/or for impregnation. Namely, these porous structures could be impregnated e.g. with a bioactive polymer, in order to obtain composite surfaces having peculiar properties, such as enhanced bioactivity coupled to anti-bacterial properties. In the

case of the SPS process, care has to be taken in order to avoid overheating effects such as those leading to the structure of sample #1, which is excessively thick and brittle and, therefore, of little practical use.

3.1.3 Phase composition of the bioactive glass coatings

As far as the phase composition is concerned, all SPS samples but #1 are mainly glassy, as seen both from XRD patterns (Fig. 8(a)) and from micro-Raman spectra (Fig. 8(c)). The only crystalline diffraction peaks are indeed those of rutile from the underlying TiO_2 bond coat, as the low thickness and low density of the SPS glass layers allow penetration of the X-rays down to the underlying surface. The HVSFS coatings (Fig. 8(b)) are also mainly glassy, with minor diffraction peaks of the pseudo-wollastonite phase ($Ca_3(Si_3O_9)$), probably formed due to slight recrystallisation inside the heated glass droplets. The micro-Raman spectra of the SPS and HVSFS samples (Fig. 8(c)) are accordingly analogous to those of SiO_2-P_2O_5-based bioactive glasses [82,83], featuring broad bands at about 615 cm^{-1}, 1020 cm^{-1} and 1070 cm^{-1}, ascribable to vibrations modes of Si–O–Si bonds in silica tetrahedra [82,84], and an intense band at about 950 cm^{-1}, ascribable to the vibration of the PO_4^{3-} group [82,85]. In the spectra of the HVSFS samples, some sharp peaks, which refer to few crystallised areas, can be observed e.g. in Fig. 8(c), spectrum 2.

The formation of wollastonite in response to the thermal treatment has been previously observed in BG-Ca/Mix based composites [70]. Differently from conventional bioactive glasses, where the development of sodium- and potassium-calcium silicates is prevalent due to the relatively higher amount of alkaline elements [86-88], the particular composition of the BG-Ca/Mix glass, low in alkaline oxides and richer in calcium oxide, favours the formation of calcium silicates. Anyway, the formation of pseudo-wollastonite is not *a priori* detrimental, since the bioactivity of this phase has been previously demonstrated by several investigations [89,90].

The only exception to the above considerations is the SPS sample #1, which recrystallised and developed substantial amounts of pseudo-wollastonite because of its prolonged permanence at temperatures significantly higher than T_g, as discussed previously.

3.2 Structure and microstructure – hydroxyapatite coatings

3.2.1 Characterisation of the reference APS HA coating

The reference HA coating of ≈50 μm thickness, deposited by conventional atmospheric plasma spraying (APS) as described in Section 2.2, exhibits a quite irregular morphology, with pores and inhomogeneities (Fig. 9(a)). This confirms that the conventional process is badly suited to the deposition of thin layers with high quality and homogeneity. In detail, the coating consists of large splats with slightly different backscattered electron contrast (Fig. 9(b)), reflecting the existence of both crystalline and amorphous lamellae. The coarse splat structure is also seen on fracture surfaces (Fig. 9(c)). The coating clearly contains some unmelted material (Fig. 9(d)), which probably corresponds to some of the brighter, crystalline areas in the polished cross-sections. Accordingly, micro-Raman spectra confirm that some areas on the cross-section of the APS coating consist of amorphous calcium phosphate only (Fig. 10, spectrum 1), whereas others consist of crystalline phases (spectrum 2). The latter comprise not only crystalline HA, but also some tricalcium phosphate (TCP) or tetracalcium phosphate (TTCP), as clearly witnessed by the presence of two distinct peaks at 951 and 960 cm^{-1}, i.e. the characteristic splitting of the v_1 vibration mode of the PO_4^{3-} tetrahedral unit occurring in TCP and TTCP [91,92]. This means some crystalline phase change occurred during spraying: this may either come from alteration of unmelted HA as the temperature overcame the decomposition threshold (without exceeding the melting point), or from incomplete recrystallisation of the liquid phase in some fully melted splats.

3.2.2 Microstructure of the HVSFS HA coatings

The HVSFS HA coating has a completely different microstructure, much denser and more homogeneous, with a thickness of about 30 μm (Fig. 11), consistent with the previous results in [31], where the deposition parameters for this type of coatings were optimised. The coating contains almost no porosities but exhibits periodic transverse microcracks (Fig. 11(a)). These were developed because of the tensile quenching stresses, which arose as the layer (deposited with a single torch cycle, Table 2) cooled down from the solidification temperature to the equilibrium surface temperature. These transverse cracks, however, should not be considered as an undesirable feature, as they do not compromise the functionality of the coating, which is not intended as an impermeable barrier, and they may even be beneficial for its compliance against substrate deformation and/or temperature variations in service.

The splat structure is much finer than that of the APS reference (compare Fig. 11(c) to Fig. 9(b)); accordingly, splats are so tightly sintered together that they are almost unidentifiable on fracture surfaces (Fig. 12(a, b)). This can be ascribed to the high velocity impact of hot, molten particles, which can flatten extensively and adhere strongly to one another. Interlamellar sintering seems to be even more complete than that of most BG-Ca/Mix samples (compare to Fig. 6). This is probably due to two factors. On the one hand, the lower viscosity of the phosphate melt compared to a silicate-based glass (which tends to retain somewhat higher viscosity even at high temperatures) allows more extensive flattening. On the other hand, the HA suspension releases small nanoparticle aggregates, which eventually turn into finer molten droplets than those seen with the micrometric glass powder. The lamellae in the HA coating (Fig. 12(d)) are therefore smaller than those of the BG-Ca/Mix coatings (Fig. 6(b, d)). These finer lamellae can flatten more easily and are more prone to sintering.

3.2.3 Microstructure of the SPS HA coatings

The microstructure of the SPS samples is completely different: analogous to the SPS bioactive glass coatings, these samples are highly porous, rough, with a columnar-like growth structure (Fig. 13). All previous considerations clearly apply to this case as well.

Again, very fine splats are recognisable (Fig. 14(a)), indicating that, in most cases, the molten HA droplets produced during the SPS process, coming from fine aggregates of primary nanoparticles, are not much different from those seen in the HVSFS process (Fig. 11). In the SPS process, however, the deflection they undergo because of their lower in-flight velocity (as discussed extensively in the case of the BG-Ca/Mix coatings, Section 3.1.1) often resulted in limited flattening, giving rise to rounded inclusions (Fig. 14(a)) which are obvious sources of defects. Even more importantly, most of the deflected particles attached preferentially onto prominent substrate asperities, giving rise to the columnar-like growth morphology, as discussed in Section 3.1.1.

In addition, large molten aggregates are sometimes produced during the SPS process (Fig. 14(b)). They are another source of defectiveness in the SPS coatings and may further promote columnar growth mechanisms by providing additional protuberances. They clearly originated from large, poorly fragmented suspension drops. This may be due to non-uniformities in the fragmentation process of the injected suspension stream. The radial injection method, which results in quite different liquid drop sizes and trajectories [42,43], and the typical voltage fluctuations of plasma torches operated with Ar-H_2 gas mixtures, which cause unstable plasma flow conditions [44], could be the main reasons for this non-uniformity.

3.2.4 Phase composition of the HA coatings

Concerning the phase composition, the HVSFS coating contains high amounts of glassy phase, as proven both by Raman spectra (Fig. 15(a)) and by XRD patterns (Fig. 16). The rapid quenching of the very fast-impinging lamellae, together with the fact that the surface temperature of the system during deposition is too low to allow recrystallisation (Table 2), indeed account for the formation of

a mainly amorphous HVSFS coating. Crystalline areas are only occasionally found (Fig. 15(a), spectrum 6), probably corresponding to some unmelted inclusions (such as the aggregate of unmelted nanoparticles seen in Fig. 12(c)).

The SPS coatings consist of a mixture of amorphous materials and of crystalline HA, TCP and TTCP, identifiable both by the multiple Raman peaks at about 960 cm^{-1} (Fig. 15(b)) [91,92] and by the XRD patterns of Fig. 17. A slight amorphous band and the peaks of TTCP and of α- and β-TCP are indeed recognisable in addition to those of the HA phase. All of these crystalline phases may have developed from the originally amorphous melt because of recrystallisation of the deposited material, which remained at an average surface temperature higher than that found during the HVSFS process (compare Table 1 and Table 2).

3.3 Bioactivity evaluation in Simulated Body Fluid

The apatite-forming ability of the coatings was evaluated *in vitro* in SBF, according to the protocol originally proposed by Kokubo et al. [72,93]. A model to describe the complicated mechanism leading to the apatite precipitation and crystallisation on the Bioglass® surface can be found in [94-96]. The debate on the topic is still open in the literature [97,98] and the results of SBF tests should be interpreted with great attention (i.e. the use of SBF for bioactivity testing may produce false-positive and false-negative results [99,100]). However, the formation of a HA layer onto the sample surface *in vitro* is usually considered as a preliminary requirement for the development of such a layer also *in vivo* [101], where it is expected to mediate a chemical bond with the surrounding bone tissue, thus favouring early bone formation at the coating-bone interface [94].

The soaking tests clearly confirm the different *in vitro* reactivity of the SPS and HVSFS bioactive glass coatings (Fig. 18). In the latter, the surface starts to turn into a silica gel layer by ion leaching and ion exchange mechanisms (Fig. 18(b)) after 1 day of soaking. XRD patterns (Fig. 19(a)) indeed show a secondary glass band around $2\theta = 23°$, belonging to the silica gel, in addition to the original

glass band centred around $2\theta = 30°$ (Fig. 20 (a, b)). After 3 days of soaking, the silica gel layer has grown thicker and a HA layer (a few micrometres in thickness) precipitated onto its surface (Fig. 18(d)), as confirmed by the appearance of diffraction peaks of HA in the corresponding XRD patterns (Fig. 19(a)). The breadth of these peaks also reveals the presence of structural defects, such as carbonate groups substituting for phosphate ones. For increasingly long soaking times, the conversion of the glass layer into a silica gel continues and the HA layer on the top surface grows further, as seen in the XRD patterns of Fig. 19(a).

The SPS coatings are not much affected after 1 day of soaking (Fig. 18(a), 19(b)). After 3 days, the broad diffraction band of the silica gel and the peaks of precipitated HA are seen in the XRD pattern (Fig. 19(b)): SEM observation of the cross-section shows that, different from the HVSFS samples, the conversion into silica gel affects practically the entire coating thickness (Fig. 18(c)). This is most likely due to the high porosity of these systems, resulting in a larger active surface for the ion leaching process. After 7 days, the XRD patterns show more extensive conversion to HA (Fig. 19(b)), but inspection of the coatings indicates that they have lost their mechanical integrity and they have started to dissolve in the solution. It is therefore confirmed that the porous SPS bioactive glass coatings are rapidly resorbable layers (as anticipated in Section 3.1.1), whereas the HVSFS coatings react more slowly, due to their lower porosity. It is even inferable that multi-layered systems can be proposed, where a more porous SPS layer can be deposited onto a more stable HVSFS coating in order to fasten the short-term reactivity on the surface while preserving the long-term stability at the interface with the substrate.

The possibility to tailor the reactivity of the BG-Ca/Mix coatings by changing their microstructure through a proper selection of the deposition process is a very advantageous feature. In particular, the specific composition of this glass makes it possible to produce denser HVSFS coatings as compared to other kinds of bioactive glasses [35,73], in accordance with the observations in Section 3.1.1.

The HVSFS HA sample also dissolves progressively into the SBF, due to its predominantly glassy structure, and starts developing a re-precipitated HA layer onto its surface after 3 days of soaking (Fig. 20 (b, d)). This is also clear from the XRD patterns (Fig. 21 (a)). The phosphate glass band and the TCP and TTCP peaks indeed tend to disappear as the newly formed HA layer (whose diffraction peaks are much broader than those of the pre-existing crystalline hydroxyapatite) replaces the original coating and covers it.

In comparison, the SPS coatings are somewhat more crystalline, hence they are intrinsically less reactive, but they possess a larger specific surface area because of their great porosity. As a result, the coatings do not develop a re-precipitated HA layer onto their surface: by contrast, a clear reduction in porosity occurs during soaking (compare Fig. 20 (a,c) to Fig. 13, where the as-deposited microstructures are shown). In fact, as the amorphous phase of the coating starts to dissolve, the apatite that re-precipitates from the SBF gradually fills in the pores, in accordance with the previous investigation in [102]. Due to the lack of a re-precipitated surface layer, changes to the XRD pattern of SPS HA samples (Fig. 21(b)) are less marked than those seen for the HVSFS samples in Fig. 19. The decreasing intensity of the TCP peaks, however, reveals that the overall amount of HA in the coatings is increasing.

The apatite precipitation on all samples after soaking in SBF has been further confirmed by Raman spectroscopy. Some representative Raman spectra acquired on the surface of BG-Ca/Mix samples and HA samples after 7 days in SBF are shown in Fig. 22. Regardless of the sample nature, the spectra are rather similar to each other and the peak positions match with those expected for crystalline HA. Multiple peaks at about 430 cm^{-1} and 590 cm^{-1} and a pronounced peak at 960 cm^{-1}, ascribable to the vibration modes of the PO_4^{3-} group of HA [103], are indeed recognisable. Moreover, the Raman spectra show a peak at about 1070 cm^{-1}, which can be associated to the stretching of carbonate groups [104]. For this reason, the deposits on the samples after soaking in SBF can be further identified as carbonated HA.

4. Conclusions

This paper compared the properties of K_2O-Na_2O-CaO-P_2O_5-SiO_2 bioactive glass coatings and of hydroxyapatite coatings obtained by two different suspension spraying processes, namely High Velocity Suspension Flame Spraying (HVSFS) and Suspension Plasma Spraying (SPS).

The analysis revealed that, in all cases, the SPS process produces highly porous, rough coatings with columnar-like growth morphology. Experimental evidence suggests that most of the incoming particles had low normal velocity and acquired a certain tangential velocity component because of the deflection by the stagnation flow in front of the substrate.

Porous bioactive glass coatings by SPS are highly reactive in simulated body fluid (SBF); hence, they behave as rapidly resorbable layers. They may also be useful as porous supports for impregnation with similarly bioresorbable compounds (e.g. functional bioactive polymers).

Porous HA layers by SPS can also have similar purpose. They however possess higher stability and lower dissolution rate. This follows from the formation of crystalline phases in the deposited material because of the quite high surface temperature of the system during deposition. Interestingly, in this case, the dissolution of the amorphous calcium phosphate fraction during soaking in SBF induces re-precipitation of HA not on top of the coating but inside its pores. Pre-treatment of this layer in SBF could therefore be proposed as a means to seal its porosity and tune its phase composition.

HVSFS deposition of bioactive glass and of HA, by contrast, always produces very dense, thin layers (<50 μm thick). The process is therefore useful when a thin, high-quality bioactive coating is needed to favour osseointegration of a metallic prosthetic implant. Well-flattened lamellae, tightly bound to one another, are evidence of the much higher impact velocity of the molten droplets.

Specifically, the HVSFS bioactive glass layers react slower than the SPS ones when immersed in the SBF, due to their much lower specific surface area. The reaction proceeds by conversion of the coating surface into a silica gel, onto which a HA layer precipitates. The HVSFS HA layer, by

contrast, is more reactive than the SPS ones in the SBF because of its much higher content of amorphous calcium phosphate phase (due to the lower surface temperature during deposition, which limits the recrystallisation of the amorphous as-deposited material). This coating tends to dissolve progressively and to be replaced by a new, re-precipitated HA layer, characterised by a more defective lattice structure.

Acknowledgements

The work was supported by the German-Italian University Centre, "Vigoni" program for international exchange (2011 call), project title: "Advanced thermally sprayed coatings for biomedical applications" (http://www.ateneoitalotedesco.org/user/0900_Doc/20131029124547PV%202011_Elenco%20progetti%20selezionati.pdf).

References

[1] M. Geetha. A.K. Singh, R. Asokamani, A.K. Gogia, Ti based biomaterials, the ultimate choice for orthopaedic implants – A review, Prog. Mater. Sci. 54 (2009) 397-425.

[2] F. Guillemot, Recent advances in the design of titanium alloys for orthopedic applications, Expert Rev. Med. Devices 2 (2005) 741-748.

[3] M. Niinomi, Mechanical biocompatibilities of titanium alloys for biomedical applications, J. Mech. Behav. Biomed. Mater. 1 (2008) 30-42.

[4] H.J. Rack, J.I. Qazi, Titanium alloys for biomedical applications, Mater. Sci. Eng. C 26 (2006) 1269-1277

[5] X. Liu, P.K. Chu, C. Ding, Surface modification of titanium, titanium alloys, and related materials for biomedical applications, Mater. Sci. Eng. R 47 (2004) 49-121.

[6] L.L. Hench, Bioceramics: from concept to clinic, J. Am. Ceram. Soc. 74 (1991) 1487–1510

[7] S.V. Dorozhkin, Calcium Orthophosphates in Nature, Biology and Medicine, Mater. 2 (2009) 399-498.

[8] K.H. Kim, R. Narayanan, T.R. Rautray, "Surface Modification of Titanium for Biomaterial Applications", in: Biomaterials: Properties, Production and Devices, Nova Science Publishers, Hauppauge, NY, USA, 2010-

[9] L. Sun, C.C. Berndt, K.A. Gross, A. Kucuk, Material fundamentals and clinical performance of plasma-sprayed hydroxyapatite coatings: a review, J. Biomed. Mater. Res. 58 (2001) 570-592

[10] C. García, S. Ceré, A. Durán, Bioactive coatings deposited on titanium alloys, J. Non-Cryst. Solids 352 (2006) 3488–3495

[11] E. Gyorgy, S. Grigorescu, G. Socol, I.N. Mihailescu, D. Janackovic, A. Dindune, Z. Kanepe, E. Palcevskis, E.L. Zdrentu, S.M. Petrescu, Bioactive glass and hydroxyapatite thin films obtained by pulsed laser deposition, Appl. Surf. Sci. 253 (2007) 7981–7986

[12] Y. Yang, K.H. Kim, J.L. Ong, A review on calcium phosphate coatings produced using a sputtering process—an alternative to plasma spraying, Biomater. 26 (2005) 327–337

[13] A. Sola, D. Bellucci, V. Cannillo, A. Cattini, Bioactive glass coatings: a review, Surf. Eng. 27 (2011) 560–572

[14] M.F. Hsieh, L.H. Perng, T.S. Chin, Hydroxyapatite coating on Ti6A14V alloy using a sol–gel derived precursor, Mater. Chem. Phys. 74 (2002) 245–250.

[15] M. Hamdi, A.M. Ektessabi, Electron beam deposition of thin bioceramic film for biomedical implants. Thin Solid Films 398 (2001) 385–390.

[16] Y.C. Tsui, C. Doyle, T.W. Clyne, Plasma sprayed hydroxyapatite coatings on titanium substrates Part 1: Mechanical properties and residual stress levels, Biomater. 19 (1998) 2015-2029.

[17] Y.C. Tsui, C. Doyle, T.W. Clyne, Plasma sprayed hydroxyapatite coatings on titanium substrates Part 2: optimisation of coating properties, Biomater. 19 (1998) 2031-2043.

[18] R.B. Heimann, Thermal spraying of biomaterials, Surf. Coat. Technol. 201 (2006) 2012–2019.

[19] P. Cheang, K.A. Khor, Addressing processing problems associated with plasma spraying of hydroxyapatite coatings, Biomater. 17 (1996) 537-544.

[20] L. Sun, C.C. Berndt, K.A. Khor, N.H. Cheang, K.A. Gross, Surface characteristics and dissolution behavior of plasma-sprayed hydroxyapatite coating, J. Biomed. Mater. Res. 62 (2002) 228-236

[21] S. Dyshlovenko, L. Pawlowski, P. Roussel, D. Murano, A. Le Maguer, Relationship between plasma spray operational parameters and microstructure of hydroxyapatite coatings and powder particles sprayed into water, Surf. Coat. Technol. 200 (2006) 3845-3855.

[22] K. de Groot, J.G.C. Wolke, J.A. Jansen, Calcium phosphate coatings for medical implants. Proc. Inst. Mech. Eng. Part H: J. Eng. Med. 212 (1998) 137-147.

[23] X. Zheng, M. Huang, C. Ding, Bond strength of plasma-sprayed hydroxyapatite/Ti composite coatings, Biomater. 21 (2000) 841-849

[24] L. Pawlowski, Suspension and solution thermal spray coatings, Surf. Coat. Technol. 203 (2009) 2807–2829

[25] A. Killinger, R. Gadow, G. Mauer, A. Guignard, R. Vaßen, D. Stöver, Review of new developments in suspension and solution precursor Thermal Spray Processes, J. Therm. Spray Technol. 20 (2011) 677-695.

[26] F.L. Toma, L.M. Berger, T. Naumann, S. Langner, Microstructures of nanostructured ceramic coatings obtained by suspension thermal spraying, Surf. Coat. Technol. 202 (2008) 4343–4348.

[27] A.R. Boccaccini, S. Keim, R. Ma, Y. Li, I. Zhitomirsky, Electrophoretic deposition of biomaterials, J. R. Soc. Interface 236 (2010) S581-613.

[28] I. Corni, M.P. Ryan, A.R. Boccaccini, Electrophoretic deposition: From traditional ceramics to nanotechnology, J. Eur. Ceram. Soc. 28 (2008) 1353-1367.

[29] A.R. Boccaccini, I. Zhitomirsky, Application of electrophoretic and electrolytic deposition techniques in ceramics processing, Curr. Opin. Solid State Mater. Sci. 6 (2002) 251-260.

[30] A. Killinger, M. Kuhn, R. Gadow, High-Velocity Suspension Flame Spraying (HVSFS), a new approach for spraying nanoparticles with hypersonic speed, Surf. Coat. Technol. 201 (2006) 1922-1929.

[31] G. Bolelli, D. Bellucci, V. Cannillo, L. Lusvarghi, A. Sola, N. Stiegler, P. Müller, A. Killinger, R. Gadow, L. Altomare, L. De Nardo, Suspension thermal spraying of hydroxyapatite: Microstructure and in vitro behaviour, Mater. Sci. Eng. C 34 (2014) 287–303.

[32] N. Stiegler, D. Bellucci, G. Bolelli, V. Cannillo, R. Gadow, A. Killinger, L. Lusvarghi, A. Sola, High Velocity Suspension Flame Sprayed (HVSFS) Hydroxyapatite Coatings for Biomedical Applications, J. Therm. Spray Technol. 21 (2012) 275-287.

[33] E. Dongmo, A. Killinger, M. Wenzelburger, R. Gadow, Numerical approach and optimization of the combustion and gas dynamics in High Velocity Suspension Flame Spraying (HVSFS), Surf. Coat. Technol. 203(15) (2009) 2139–2145.

[34] G. Bolelli, N. Stiegler, D. Bellucci, V. Cannillo, R. Gadow, A. Killinger, L. Lusvarghi, A. Sola, Deposition mechanisms in high velocity suspension spraying: Case study for two bioactive materials, Surf. Coat. Technol. 210 (2012) 28-45.

[35] L. Altomare, D. Bellucci, G. Bolelli, B. Bonferroni, V. Cannillo, L. De Nardo, R. Gadow, A. Killinger, L. Lusvarghi, A. Sola, N. Stiegler, Microstructure and in vitro behaviour of 45S5 bioglass coatings deposited by high velocity suspension flame spraying (HVSFS), J. Mater. Sci.: Mater. Med. 22 (2011) 1303–1319

[36] S. Lopez-Esteban, E. Saiz, S. Fujino, T. Oku, K. Suganuma, A.P. Tomsia, Bioactive glass coatings for orthopedic metallic implants, J. Eur. Ceram. Soc. 23 (2003) 2921–2930.

[37] A. Sola, D. Bellucci, V. Cannillo, A. Cattini, Bioactive glass coatings: a review, Surf. Eng. 27 (2011) 560–572.

[38] S. Foppiano, S.J. Marshall, G.W. Marshall, E. Saiz, A.P. Tomsia, Bioactive glass coatings affect the behavior of osteoblast-like cells, Acta Biomater. 3 (2007) 765–771.

[39] J. Schrooten, J.A. Helsen, Adhesion of bioactive glass coating to Ti6Al4V oral implant, Biomater. 21 (2000) 1461-1469.

[40] M. Bosetti, M. Cannas, The effect of bioactive glasses on bone marrow stromal cells differentiation, Biomater. 26 (2005) 3873–3879.

[41] R.M. Day, Bioactive Glass Stimulates the Secretion of Angiogenic Growth Factors and Angiogenesis in Vitro, Tissue Eng. 11 (2005) 768-777.

[42] P. Fauchais, R. Etchart-Salas, V. Rat, J.F. Coudert, N. Caron, K. Wittmann-Ténèze, Parameters Controlling Liquid Plasma Spraying: Solutions, Sols, or Suspensions, J. Therm. Spray Technol. 17(1) (2008) 31-59.

[43] E. Meillot, R. Vert, C. Caruyer, D. Damiani, M. Vardelle, Manufacturing nanostructured YSZ coatings by suspension plasma spraying (SPS): effect of injection parameters, J. Phys. D: Appl. Phys. 44 (2011) 19400.

[44] C. Marchand, C. Chazelas, G. Mariaux, A. Vardelle, Liquid Precursor Plasma Spraying: Modeling the Interactions Between the Transient Plasma Jet and the Droplets, J. Therm. Spray Technol. 6(5-6) (2007) 705–712.

[45] J. Krowka, V. Rat, J.F. Coudert, Resonant mode for a dc plasma spray torch by means of pressure–voltage coupling: application to synchronized liquid injection, J. Phys. D: Appl. Phys. 46 (2013) 224018.

[46] J. Krowka, V. Rat, J.F. Coudert, Investigation and control of dc arc jet instabilities to obtain a self-sustained pulsed laminar arc jet, J. Phys. D: Appl. Phys. 46 (2013) 505206.

[47] P. Fauchais, G. Montavon, R.S. Lima, B.R. Marple, Engineering a new class of thermal spray nano-based microstructures from agglomerated nanostructured particles, suspensions and solutions: an invited review, J. Phys. D: Appl. Phys. 44 (2011) 093001.

[48] C. Delbos, J. Fazilleau, V. Rat, J. F. Coudert, P. Fauchais, B. Pateyron, Phenomena Involved in Suspension Plasma Spraying. Part 2: Zirconia Particle Treatment and Coating Formation, Plasma Chem. Plasma Process. 26 (2006) 393–414.

[49] P. Fauchais, A. Joulia, S. Goutier, C. Chazelas, M. Vardelle, A. Vardelle, S. Rossignol, Suspension and solution plasma spraying, J. Phys. D: Appl. Phys. 46 (2013) 224015.

[50] M. Marr, O. Kesler, Influence of plasma heat flux on segmentation cracking and permeability of thin suspension plasma sprayed coatings, Surf. Coat. Technol. 216 (2013) 289–296.

[51] C. Delbos, J. Fazilleau, V. Rat, J.F. Coudert, P. Fauchais, L. Bianchi, Influence of powder size distribution and heat flux on yttria stabilised coatings elaborated by liquid suspension injection in a DC plasma jet, in: E. Lugscheider (Ed.), Thermal Spray connects: Explore its surfacing potential – Proceedings of the International Thermal Spray Conference 2005, DVS Verlag, Düsseldorf, Germany, 2005.

[52] P. Fauchais, R. Etchart-Salas, C. Delbos, M. Tognonvi, V. Rat, J.F. Coudert, T. Chartier, Suspension and solution plasma spraying of finely structured layers: potential application to SOFCs, J. Phys. D: Appl. Phys. 40 (2007) 2394–2406.

[53] O. Tingaud, A. Grimaud, A. Denoirjean, G. Montavon, V. Rat, J.F. Coudert, P. Fauchais, T. Chartier, Suspension Plasma-Sprayed Alumina Coating Structures: Operating Parameters Versus Coating Architecture, J. Therm. Spray Technol. 17(5-6) (2008) 662–670.

[54] O. Tingaud, G. Montavon, A. Denoirjean, J.-F. Coudert, V. Rat, P. Fauchais, Al_2O_3-ZrO_2 Finely Structured Multilayer Architectures from Suspension Plasma Spraying, J. Therm. Spray Technol. 19(1-2) (2010) 207-218.

[55] H. Podlesak, L. Pawlowski, R. d'Haese, J. Laureyns, T. Lampke, S. Bellayer, Advanced Microstructural Study of Suspension Plasma Sprayed Hydroxyapatite Coatings, J. Therma. Spray Technol. 19(3) (2010) 657-664.

[56] L. Latka, S.B. Goryachev, S. Kozerski, L. Pawlowski, Sintering of Fine Particles in Suspension Plasma Sprayed Coatings, Mater. 3 (2010) 3845-3866.

[57] P. Carpio, E. Bannier, M.D. Salvador, A. Borrell, R. Moreno, E. Sánchez, Effect of particle size distribution of suspension feedstock on the microstructure and mechanical properties of suspension plasma spraying YSZ coatings, Surf. Coat. Technol. 268 (2015) 293–297.

[58] M. Vicent, E. Bannier, P. Carpio, E. Rayón, R. Benavente, M.D. Salvador, E. Sánchez, Effect of the initial particle size distribution on the properties of suspension plasma sprayed Al_2O_3–TiO_2 coatings, Surf. Coat. Technol. 268 (2015) 209–215.

[59] J. Marthe, E. Meillot, G. Jeandel, F. Enguehard, J. Ilavsky, Explorations and 3D models of Atmospheric and Suspension Plasma Spraying coating microstructure, Surf. Coat. Technol. 268 (2015) 266–271.

[60] G. Bolelli, J. Rauch, V. Cannillo, A. Killinger, L. Lusvarghi, R. Gadow, Investigation of High-Velocity Suspension Flame Sprayed (HVSFS) glass coatings, Mater. Lett. 62(17-18) (2008) 2772-2775.

[61] Q. Wu, J. Huang, H. Li, Deposition of porous nano-WO_3 coatings with tunable grain shapes by liquid plasma spraying for gas-sensing applications, Mater. Lett. 141 (2015) 100–103.

[62] S.-L. Zhang, C.-X. Li, C.-J. Li, Chemical compatibility and properties of suspension plasma-sprayed $SrTiO_3$-based anodes for intermediate-temperature solid oxide fuel cells, J. Power Sources 264 (2014) 195–205.

[63] A. Ganvir, N. Curry , N. Markocsan, P. Nylén, F.-L. Toma, Comparative study of suspension plasma sprayed and suspension high velocity oxy -fuel sprayed YSZ thermal barrier coatings, Surf. Coat. Technol. 268 (2015) 70–76.

[64] A. Cattini, D. Bellucci, A. Sola, L. Pawłowski, V. Cannillo, Microstructural design of functionally graded coatings composed of suspension plasma sprayed hydroxyapatite and bioactive glass, J. Biomed. Mater. Res. Part B: Appl. Biomater. 102 (2014) 551–560.

[65] A. Cattini, D. Bellucci, A. Sola, L. Pawłowski, V. Cannillo, Functional bioactive glass topcoats on hydroxyapatite coatings: Analysis of microstructure and in-vitro bioactivity, Surf. Coat. Technol. 240 (2014) 110–117.

[66] A. Cattini, L. Łatka, D. Bellucci, G. Bolelli, A. Sola, L. Lusvarghi, L. Pawłowski, V. Cannillo, Suspension plasma sprayed bioactive glass coatings: effects of processing on microstructure mechanical properties and in-vitro behaviour, Surf. Coat. Technol. 220 (2013) 52–59.

[67] A. Cattini, D. Bellucci, A. Sola, L. Pawłowski, V. Cannillo, Suspension plasma spraying of optimized functionally graded coatings of bioactive glass/hydroxyapatite, Surf. Coat. Technol. 236 (2013) 118–126.

[68] D. Bellucci, A. Sola, V. Cannillo, Low Temperature Sintering of Innovative Bioactive Glasses, J. Am. Ceram. Soc. 95 (2012) 1313-1319.

[69] D. Bellucci, V. Cannillo, A. Sola, Calcium and potassium addition to facilitate the sintering of bioactive glasses, Mater. Lett. 65 (2011) 1825–1827.

[70] D. Bellucci, A. Sola, V. Cannillo, Bioactive glass-based composites for the production of dense sintered bodies and porous scaffolds, Mater. Sci. Eng. C 33 (2013) 2138–2151.

[71] A. Sola, D. Bellucci, V. Cannillo, Enamelled coatings produced with low-alkaline bioactive glasses, Surf. Coat. Technol. 248 (2014) 1–8.

[72] T. Kokubo, H. Takadama, How useful is SBF in predicting in vivo bone bioactivity? Biomater. 27 (2006)2907-2915.

[73] D. Bellucci, G. Bolelli, V. Cannillo, R. Gadow, A. Killinger, L. Lusvarghi, A. Sola, N. Stiegler, High velocity suspension flame sprayed (HVSFS) potassium-based bioactive glass coatings with and without TiO_2 bond coat, Surf. Coat. Technol. 206(19-20) (2012) 3857–3868.

[74] W.C. Oliver, G.M. Pharr, An improved technique for determining hardness and elastic modulus using load and displacement sensing indentation experiments, J. Mater. Res. 6 (1992) 1564–1583.

[75] P. Kulkarni, P.A. Baron, K. Willeke, in: P. Kulkarni, P.A. Baron, K. Willeke (Eds.), Aerosol Measurement. Principles, Techniques, and applications – Third Edition, J. Wiley & Sons Ltd., Chichester, UK, 2011, pp. 15-30.

[76] C. Qiu, Y. Chen, Manufacturing Process of Nanostructured Alumina Coatings by Suspension Plasma Spraying, J. Therm. Spray Technol. 18(2) (2009) 272-283.

[77] B. Pateyron, L. Pawłowski, N. Calve, G. Delluc, A. Denoirjean, Modeling of phenomena occurring in plasma jet during suspension spraying of hydroxyapatite coatings, Surf. Coat. Technol. 214 (2013) 86-90.

[78] J.P. Trelles , C. Chazelas, A. Vardelle, J.V.R. Heberlein, Arc Plasma Torch Modeling, J. Therm. Spray Technol. 18(5-6) (2009) 728-752.

[79] K. VanEvery, M.J.M. Krane, R.W. Trice, H. Wang, W. Porter, M. Besser, D. Sordelet, J. Ilavsky, J. Alme, Column Formation in Suspension Plasma-Sprayed Coatings and Resultant Thermal Properties, J. Therm. Spray Technol. 20(4) (2011) 817-828.

[80] J. Oberste Berghaus, S. Bouaricha, J.-G. Legoux, C. Moreau, Injection conditions and in-flight particle states in suspension plasma spraying of alumina and zirconia nano-ceramics, in: E. Lugscheider (Ed.), Thermal Spray Connects – Explore its Surfacing Potential. Proceedings of the International Thermal Spray Conference 2005, DVS Verlag, Düsseldorf, Germany, 2005.

[81] G. Bolelli, V. Cannillo, R. Gadow, A. Killinger, L. Lusvarghi, T. Manfredini, P. Müller, Properties of Al_2O_3 coatings by High Velocity Suspension Flame Spraying (HVSFS): Effects of injection systems and torch design Surf. Coat. Technol. 270 (2015) 175–189.

[82] C.C. Lin, L.C. Huang, P. Shen, $Na_2CaSi_2O_6$–P_2O_5 based bioactive glasses. Part 1: Elasticity and structure, J. Non-Cryst. Solids 351 (2005) 3195-3203.

[83] D. Bellucci, G. Bolelli, V. Cannillo, A. Cattini, A. Sola, In situ Raman spectroscopic investigation of bioactive glass reactivity: Simulated Body Fluid solution VS TRIS-buffered solution. Mater. Charact. 62 (2011) 1021–1028.

[84] E.C. Ziemath, M.A. Aegerter, Raman and infrared investigations of glass and glass-ceramics with composition $2Na_2O{\cdot}1CaO{\cdot}3SiO_2$, J. Mater. Res. 1 (1994) 216–225.

[85] A. Antonakos, E. Liarokapis, T. Leventouri, Micro-Raman and FTIR studies of synthetic and natural apatites, Biomater. 28 (2007) 3043–3054.

[86] H. Arstila, E. Vedel, L. Hupa, M. Hupa, Factors affecting crystallization of bioactive glasses, J. Eur. Ceram. Soc. 27 (2007) 1543–1546.

[87] L. Lefebvre, J. Chevalier, L. Gremillard, R. Zenati, G. Thollet, D. Bernache-Assolant, A. Govin, Structural transformations of bioactive glass 45S5 with thermal treatments, Acta Mater. 55 (2007) 3305–3313.

[88] D. Bellucci, V. Cannillo, A. Sola, An overview of the effects of thermal processing on bioactive glasses, Sci. Sinter. 42 (2010) 307–320.

[89] P.N. De Aza, Z.B. Luklinska, M.R. Anseau, F. Guitan, S. De Aza, Morphological studies of pseudowollastonite for biomedical application, J. Microsc. 182 (1996) 24–31.

[90] P.N. De Aza, F. Guitan, S. De Aza, Bioactivity of wollastonite ceramics: in vitro evaluation, Scripta Mater. 31 (1994) 1001–1005.

[91] R.G. Carrodeguas, S. De Aza, α-Tricalcium phosphate: Synthesis, properties and biomedical applications. Acta Biomater. 7 (2011) 3536-3546.

[92] U. Posset, E. Löcklin, R. Thull, W. Kiefer, Vibrational spectroscopic study of tetracalcium phosphate in pure polycrystalline form and as a constituent of a self-setting bone cement, J. Biomed. Mater. Res. 40 (1998) 640-645.

[93] T. Kokubo, H. Kushitani, S. Sakka, T. Kitsugi, T. Yamamuro, Solutions able to reproduce in vivo surface-structure changes in bioactive glass-ceramic A-W, J. Biomed. Mater. Res. 24 (1990) 721–734.

[94] L.L. Hench, Bioceramics, J. Am. Ceram. Soc. 81 (1998) 1705-1728.

[95] C.Y. Kim, A.E. Clark, L.L. Hench, Early stages of calcium-phosphate layer formation in bioglasses, J. Non-Cryst. Solids 113 (1989) 195–202.

[96] K.S.K. Lin, Y. Tseng, Y. Mou, Y. Hsu, C. Yang, J.C.C. Chan, Mechanistic Study of apatite formation on bioactive glass surface using ^{31}P Solid-State NMR Spectroscopy, Chem. Mater. 17 (2005) 4493–4501

[97] M. Bohner, J. Lemaitre, Can bioactivity be tested in vitro with SBF solution?, Biomater. 30 (2009) 2175–2179.

[98] J.T.Y. Lee, Y. Leng, K.L. Chow, F. Ren, X. Ge, K. Wang, X. Lu, Cell culture medium as an alternative to conventional simulated body fluid, Acta Biomater. 7 (2011) 2615–2622.

[99] S. Kotani, Y. Fujita, T. Kitsugi, T. Nakamura, T. Yamamuro, C. Ohtsuki, T. Kokubo, Bone bonding mechanism of α-tricalcium phosphate, J. Biomed. Mater. Res. 25 (1991) 1303–1315.

[100] D. Stubbs, M. Deakin, P. Chapman-Sheath, W. Bruce, J. Debes, R.M. Gillies, W.R. Walsh, In vivo evaluation of resorbable bone graft substitutes in a rabbit tibial defect model, Biomater. 25 (2004) 5037–5044.

[101] S. Aryal, S.R. Bhattarai, K.C. Remant Bahadur, M.S. Khil, D.R. Lee, H.Y. Kim, Carbon nanotubes assisted biomimetic synthesis of hydroxyapatite from simulated body fluid, Mater. Sci. Eng. A 426 (2006) 202–207.

[102] L. Łatka, L. Pawlowski, D. Chicot, C. Pierlot, F. Petit, Mechanical properties of suspension plasma sprayed hydroxyapatite coatings submitted to simulated body fluid, Surf. Coat. Technol. 205(4) (2010) 954-960.

[103] S. Koutsopoulos, Synthesis and characterization of hydroxyapatite crystals: A review study on the analytical methods, J. Biomed. Mater. Res. 62 (2002) 600–612.

[104] A. Awonusi, M.D. Morris, M.M.J. Tecklenburg, Carbonate Assignment and Calibration in the Raman Spectrum of Apatite, Calcif. Tissue Int. 81 (2007) 46–52.

Tables

Table 1. SPS process parameters for the deposition of the BG-Ca/Mix and HA suspensions.

Material	***BG-Ca-Mix***				***Hydroxyapatite***			
Parameter set	**#1**	**#2**	**#3**	**#4**	**#1**	**#2**	**#3**	**#4**
Ar flow rate (SL/min)	40	40	50	50	40	40	50	50
H_2 flow rate (SL/min)	10	10	10	10	10	10	10	10
Arc current (A)	600	600	600	600	600	600	600	600
Suspension feed rate (g/min)	42	42	42	42	47	47	47	47
Stand-off distance (mm)	60	60	60	80	60	60	60	80
Traverse speed (mm/s)	500	500	500	500	500	500	500	500
Pass spacing (mm)	3	3	3	3	3	3	3	3
Number of torch cycles	8	2	2	2	2	4	4	4
Max. deposition T (°C)	732	538	485	477	405	500	616	357

Table 2. HVSFS process parameters for the deposition of the BG-Ca/Mix and HA suspensions.

Material	***BG-Ca-Mix***					***Hydroxyapatite***
Parameter set	**#1**	**#2**	**#3**	**#4**	**#5**	**#1**
Propane flow rate (SL/min)	55	45	45	55	50	55
Oxygen flow rate (SL/min)	350	300	350	300	325	300
Suspension feed rate (g/min)	77	77	77	77	77	105
Stand-off distance (mm)	120	120	100	100	110	100
Traverse speed (mm/s)	600	600	600	600	600	600
Pass spacing (mm)	2	2	2	2	2	2
Number of pre-hating cycles	4	4	4	4	4	4
Number of deposition cycles	1	1	1	1	1	1
Max. deposition T (°C)	266	239	237	345	227	≈300

Table 3. APS process parameters for the deposition of the HA powder.

Parameter	**Setting**
Primary gas (Ar) flow rate (SL/min)	50
Secondary gas (H_2) flow rate (SL/min)	1
Arc current (A) x Voltage (V)	450 x 57
Powder feeding disk – revolution speed (rpm)	2
Carrier gas (Ar) flow rate (SL/min)	6
Stand-off distance (mm)	100
Traverse speed (mm/s)	600
Pass spacing (mm)	3
Number of torch cycles	6
Maximum deposition temperature (°C)	128

Table 4. Nano-indentation results for HVSFS BG-Ca/Mix samples: hardness (HV) and elastic modulus (E_{IT}).

Sample	*HVSFS #1*	*HVSFS #2*	*HVSFS #3*	*HVSFS #4*	*HVSFS #5*
HV	496 ± 124	486 ± 94	396 ± 37	617 ± 72	516 ± 92
E_{IT} [GPa]	77 ± 12	81 ± 19	61 ± 4	95 ± 5	82 ± 8

Figure captions

Figure 1. Cross-sectional SEM micrographs (backscattered electrons) of SPS BG-Ca/Mix coatings #4 (a, b), #3 (c, d), #2 (e, f) deposited onto the TiO_2 bond coat.

Figure 2. SEM micrographs (secondary electrons) of the fracture section (a, b) and of the top surface (c, d) of SPS BG-Ca/Mix sample #2.

Figure 3. Cross-sectional SEM micrographs (backscattered electrons) of SPS BG-Ca/Mix coating #1 deposited onto the TiO_2 bond coat.

Figure 4. SEM micrographs (secondary electrons) of the fracture section of SPS BG-Ca/Mix sample #1.

Figure 5. SEM micrographs (backscattered electrons) of the polished cross-sections of HVSFS BG-Ca/Mix samples #1 (a, b), #2 (c, d), #3 (e, f), #4 (g, h), #5 (i, l).

Figure 6. SEM micrographs (secondary electrons) of the fracture sections (a, c, d) and of the top surfaces (b, d, f) of HVSFS BG-Ca/Mix samples #3 (a, b), #4 (c, d), #5 (e, f).

Figure 7. SEM micrographs showing the presence of big splats on the surface of HVSFS BG-Ca/Mix sample #4: polished cross-section, backscattered electrons (a) and top surface, secondary electrons (b).

Figure 8. XRD patterns of all SPS (a) and HVSFS (b) BG-Ca/Mix coatings, and representative micro-Raman spectra of the latter (c).

Figure 9. SEM micrographs of the polished cross-section (a, b) and of the fracture section (c, d) of the atmospheric plasma sprayed HA reference.

Figure 10. Representative Raman spectra acquired at different locations on the polished cross-section of the APS HA coating.

Figure 11. Cross-sectional SEM micrographs (backscattered electrons) of the HVSFS HA sample.

Figure 12. SEM micrographs (secondary electrons) of the fracture section (a, b, c) and of the top surface (d) of the HVSFS HA coating.

Figure 13. SEM micrographs (backscattered electrons) of the polished cross-sections of SPS HA samples #3 (a, b), #4 (c, d), #5 (e, f).

Figure 14. SEM micrograph (secondary electrons) with high-magnification details of the polished cross-section of SPS HA samples #4 (a) and #3 (b).

Figure 15. Representative Raman spectra acquired throughout the cross-section of the HVSFS HA sample (a) and on the cross-section of the SPS HA sample #3 (b).

Figure 16. XRD pattern of the HVSFS HA sample. All peaks belong to crystalline HA, except where noted.

Figure 17. XRD patterns of SPS HA samples compared to a pure HA reference. All peaks belong to crystalline HA, except where noted.

Figure 18. Cross-sectional SEM micrographs (backscattered electrons) of the SPS BG-Ca/Mix sample #2 (a, c) and of the HVSFS BG-Ca/Mix sample #3 (c, d) after 1 day (a, b) and 3 days (c, d) of soaking in the simulated body fluid solution.

Figure 19. XRD patterns of the BG-Ca/Mix coatings after various soaking times in SBF: HVSFS sample #3 (a) and SPS sample #2 (b).

Figure 20. Cross-sectional SEM micrographs (backscattered electrons) of the SPS HA sample #4 (a, c) and of the HVSFS HA sample (c, d) after 1 day (a, b) and 3 days (c, d) of soaking in the simulated body fluid solution.

Figure 21. XRD patterns of the HA coatings after various soaking times in SBF: HVSFS sample (a) and SPS sample #5 (b).

Figure 22. Representative Raman spectra acquired on the surface of BG-Ca/Mix samples (a) and HA samples (b) after 7 days in SBF.

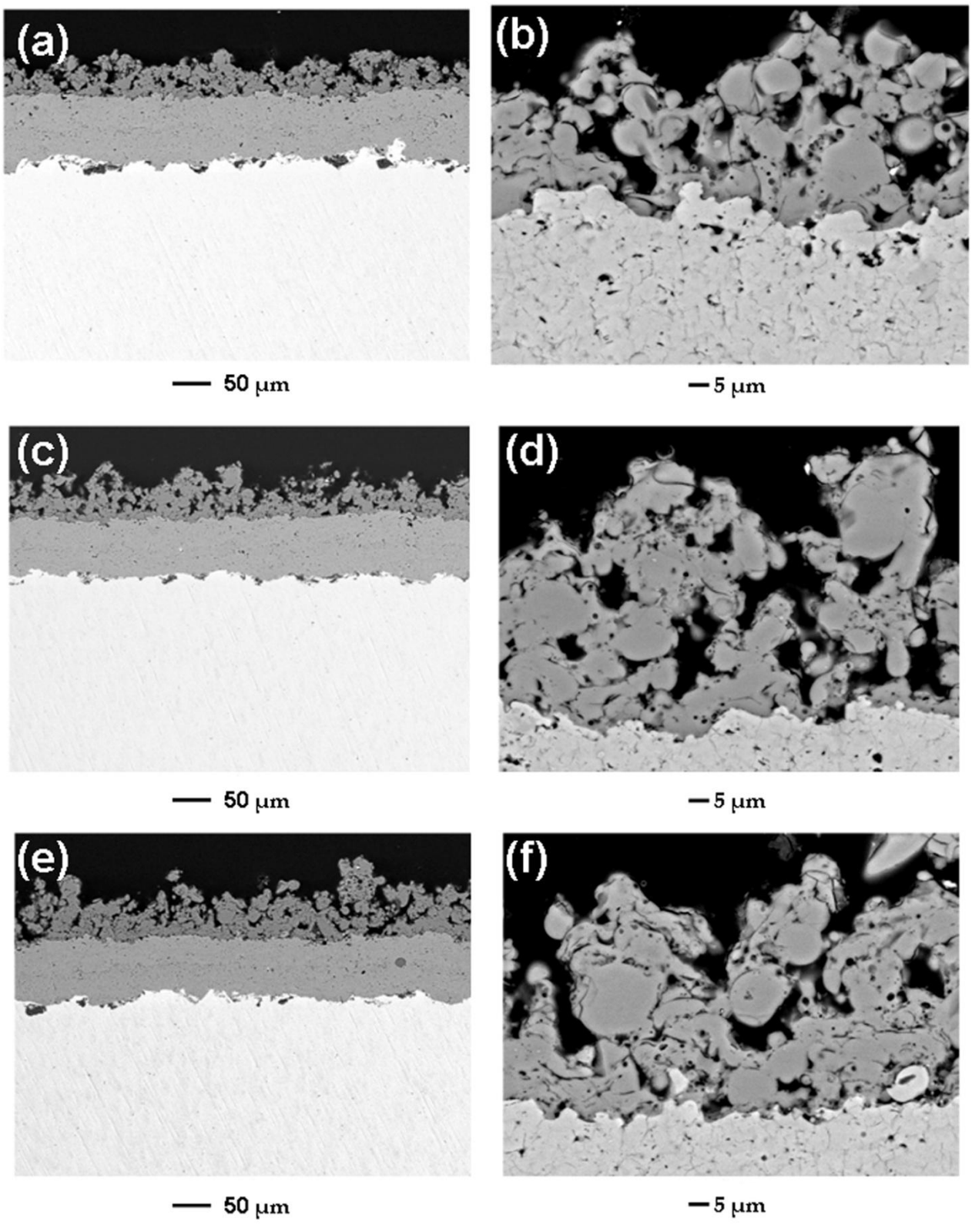

Figure 1

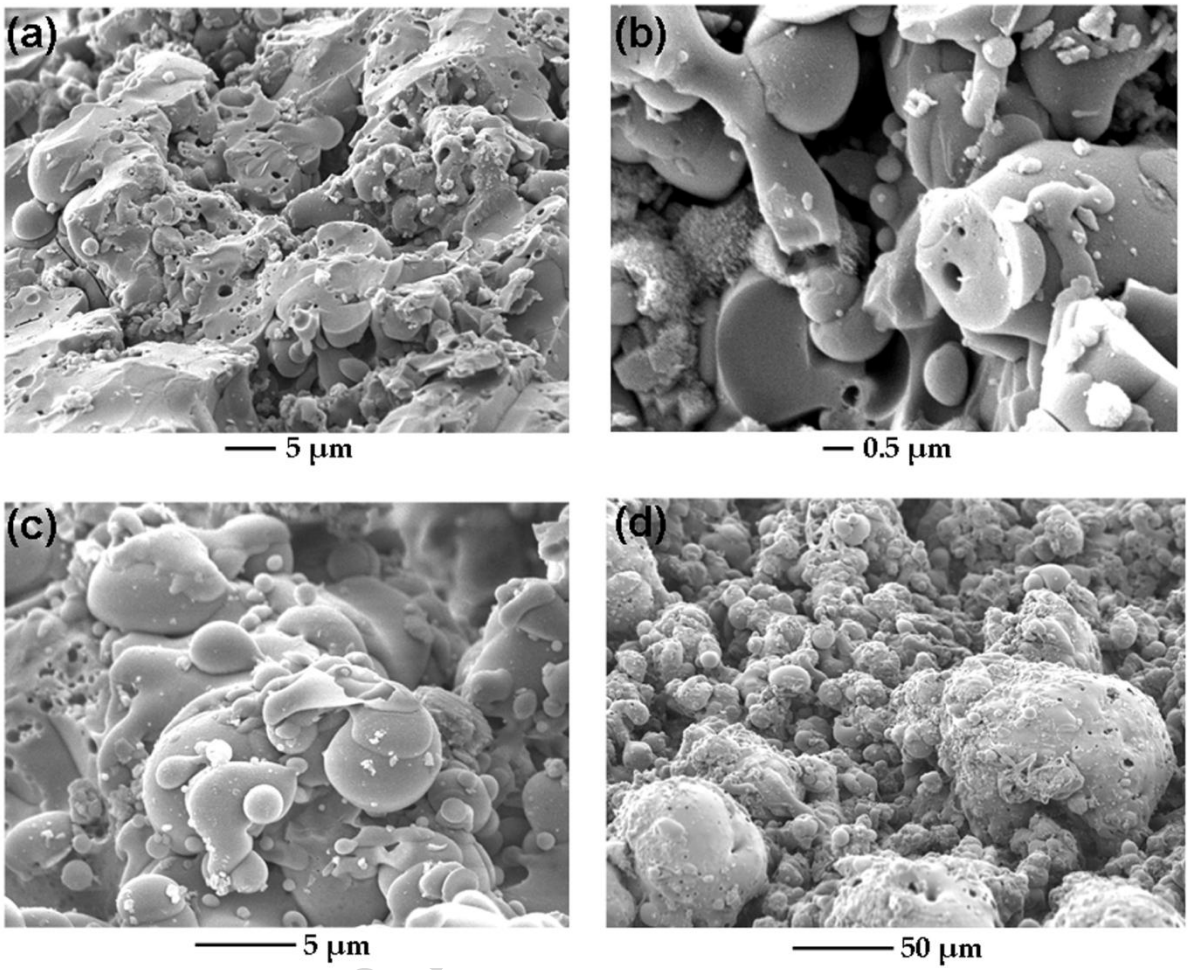

Figure 2

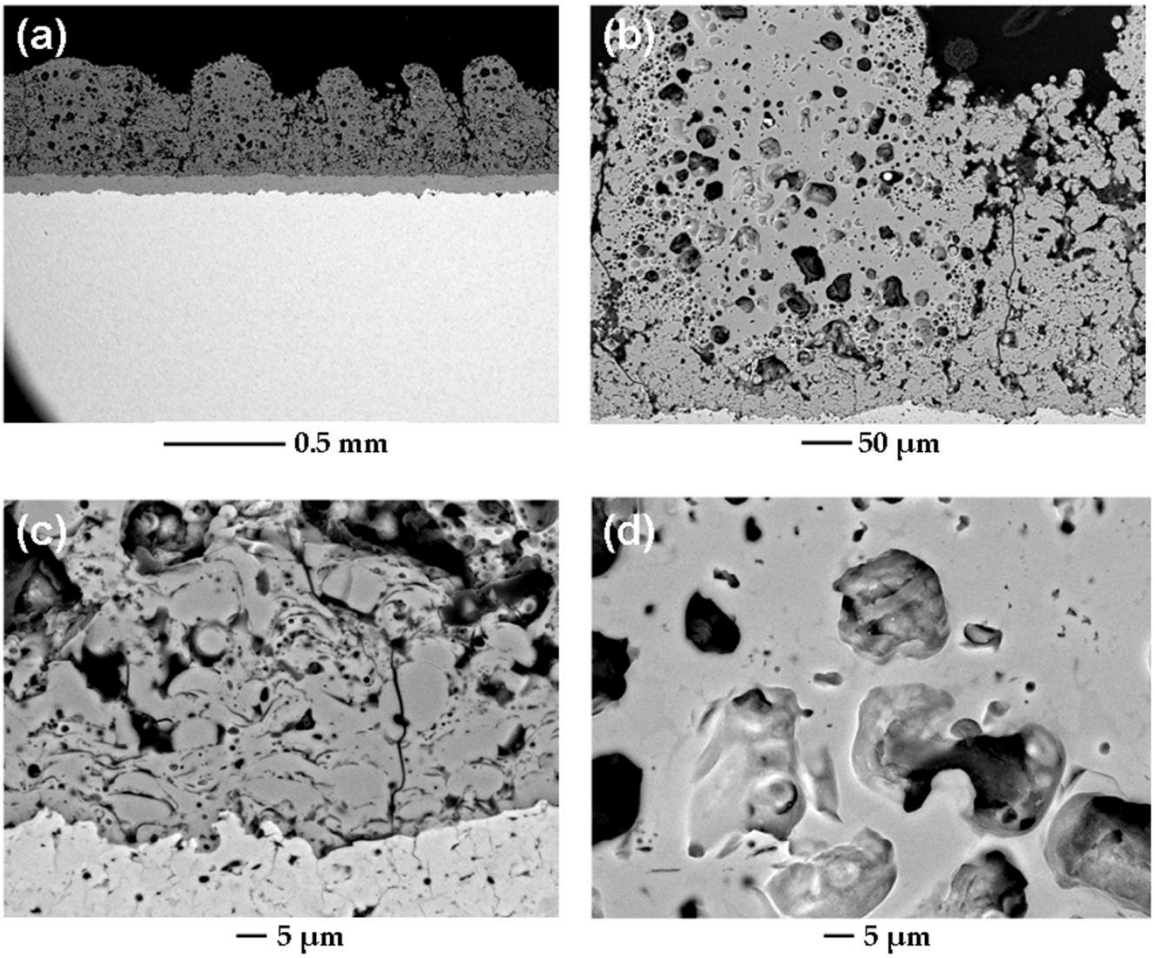

Figure 3

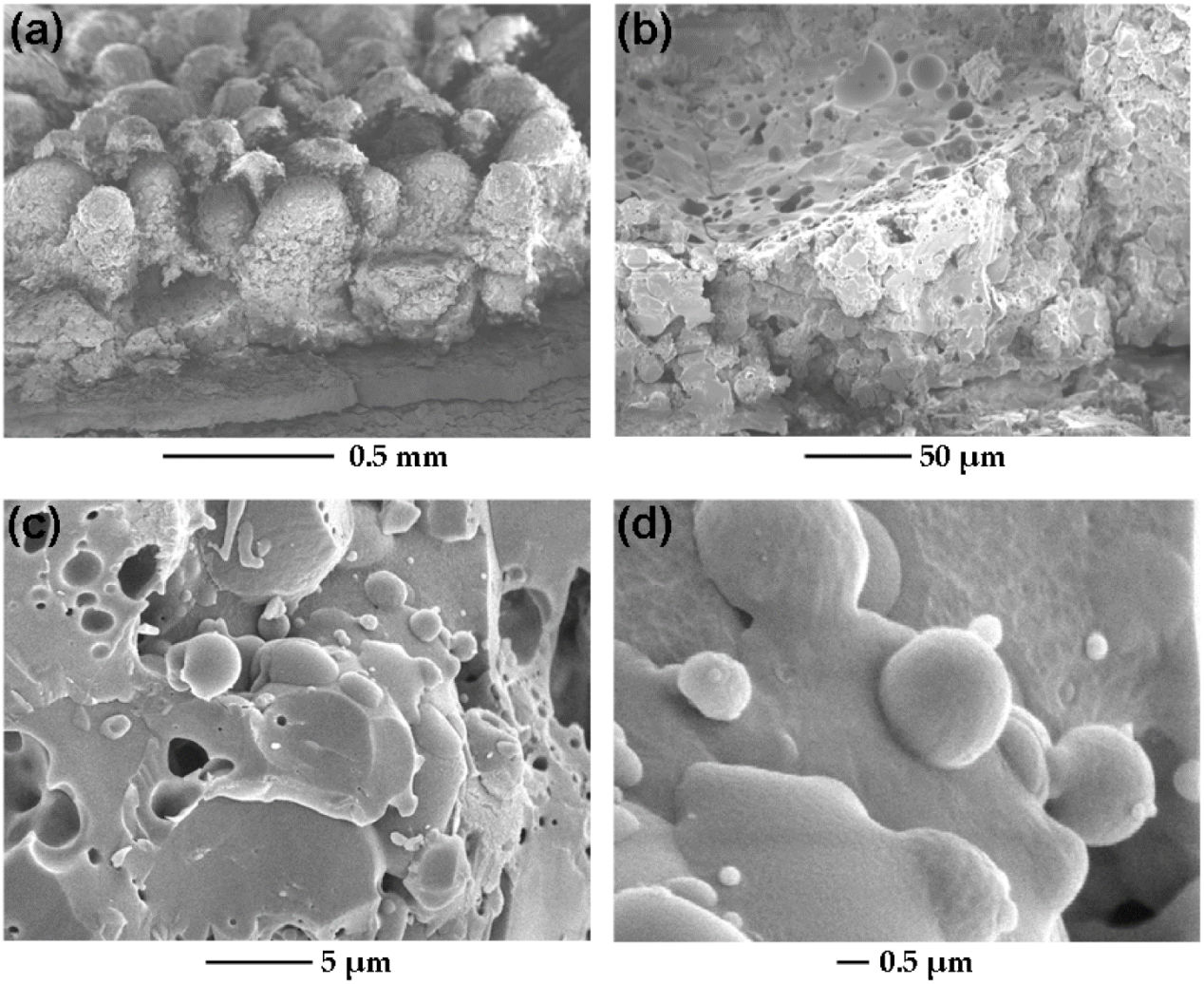

Figure 4

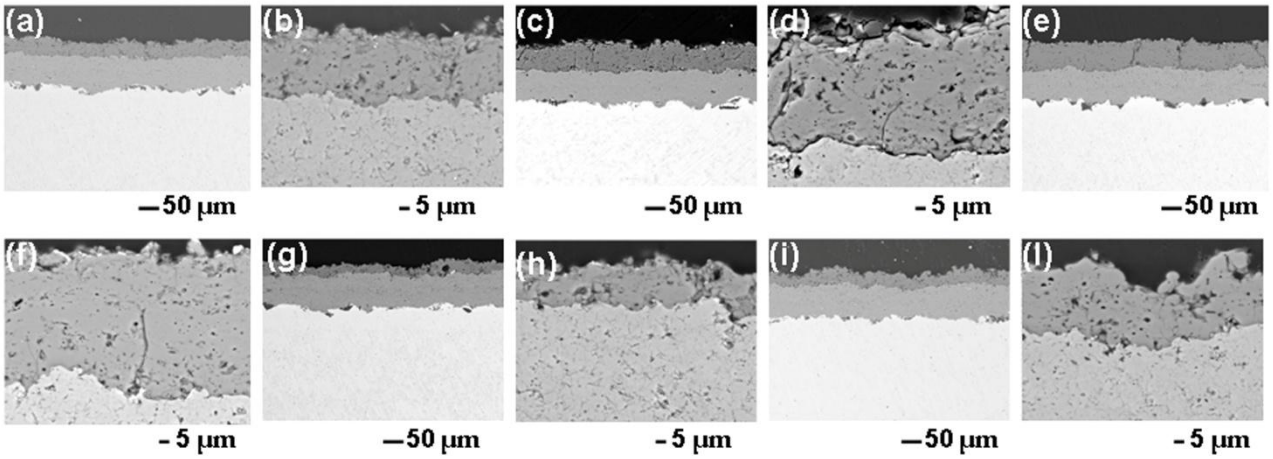

Figure 5

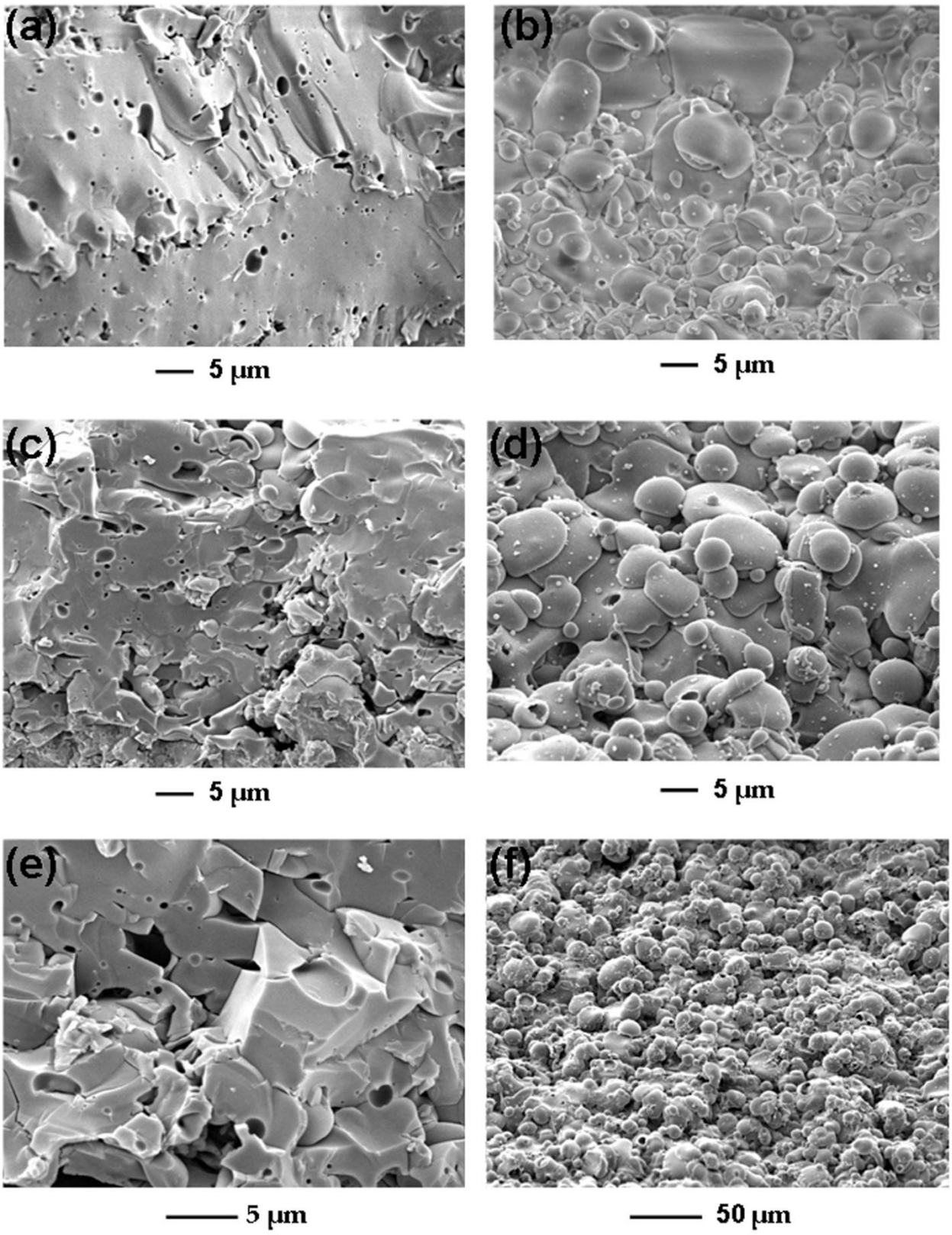

Figure 6

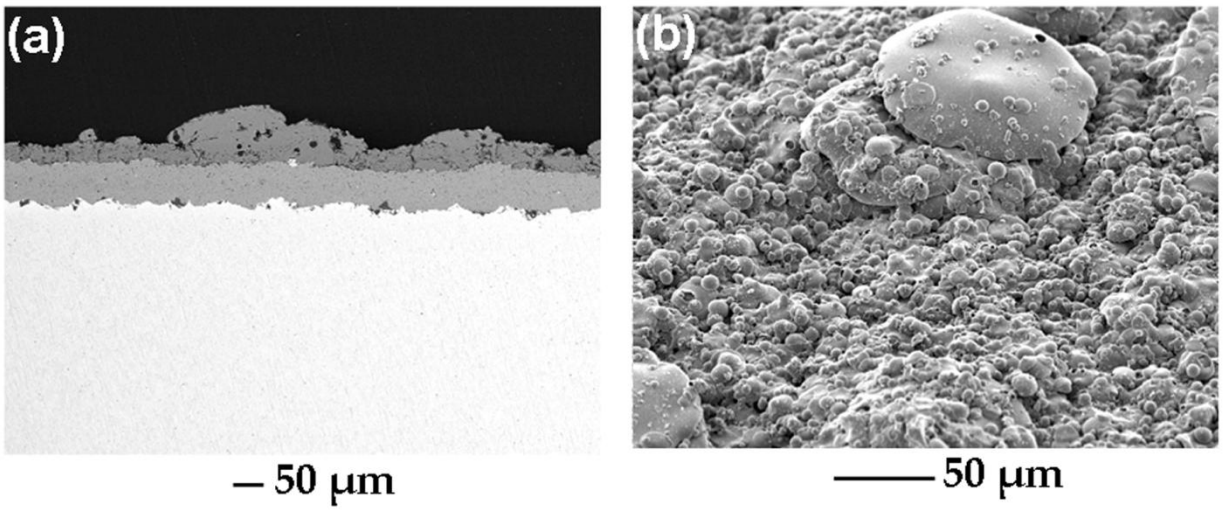

Figure 7

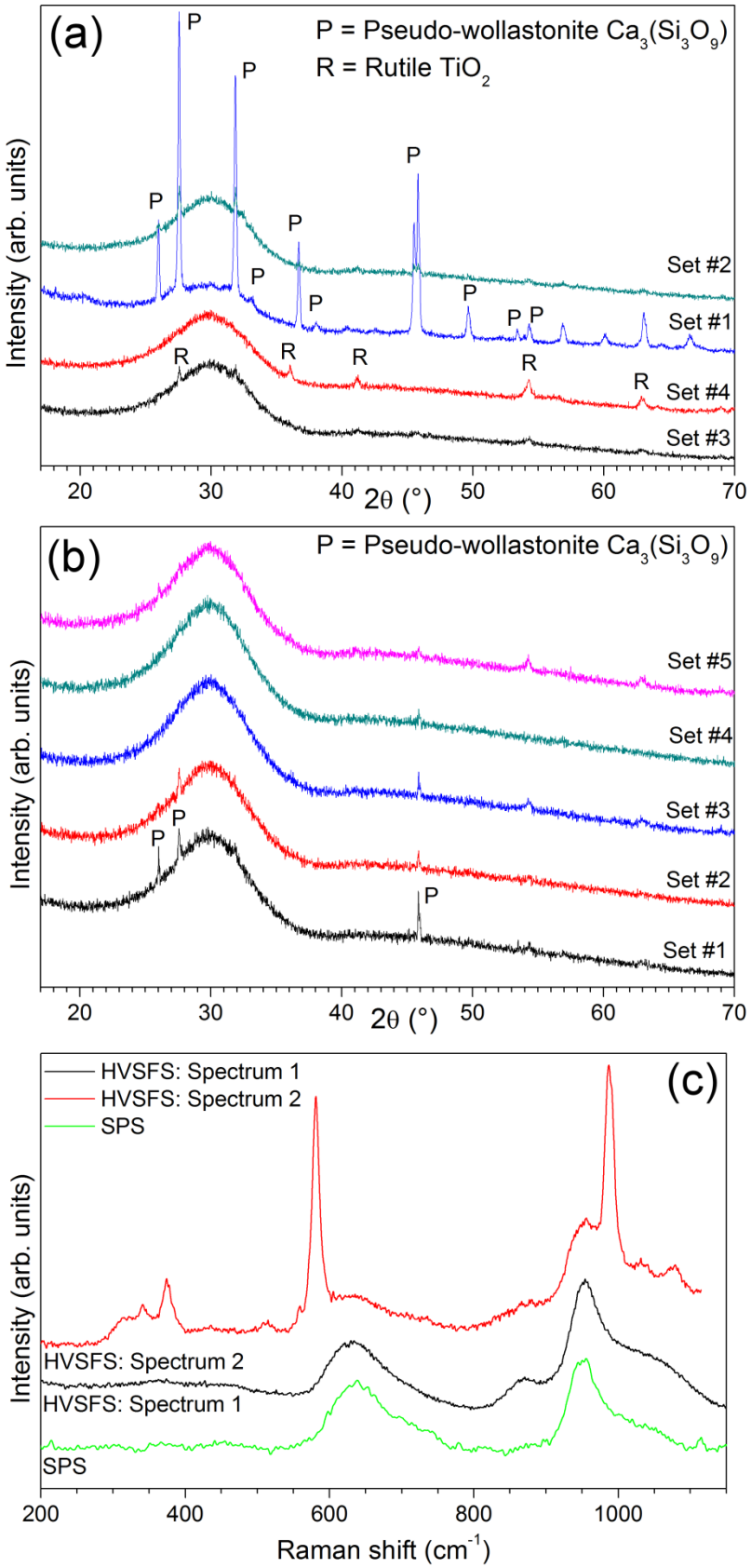

Figure 8

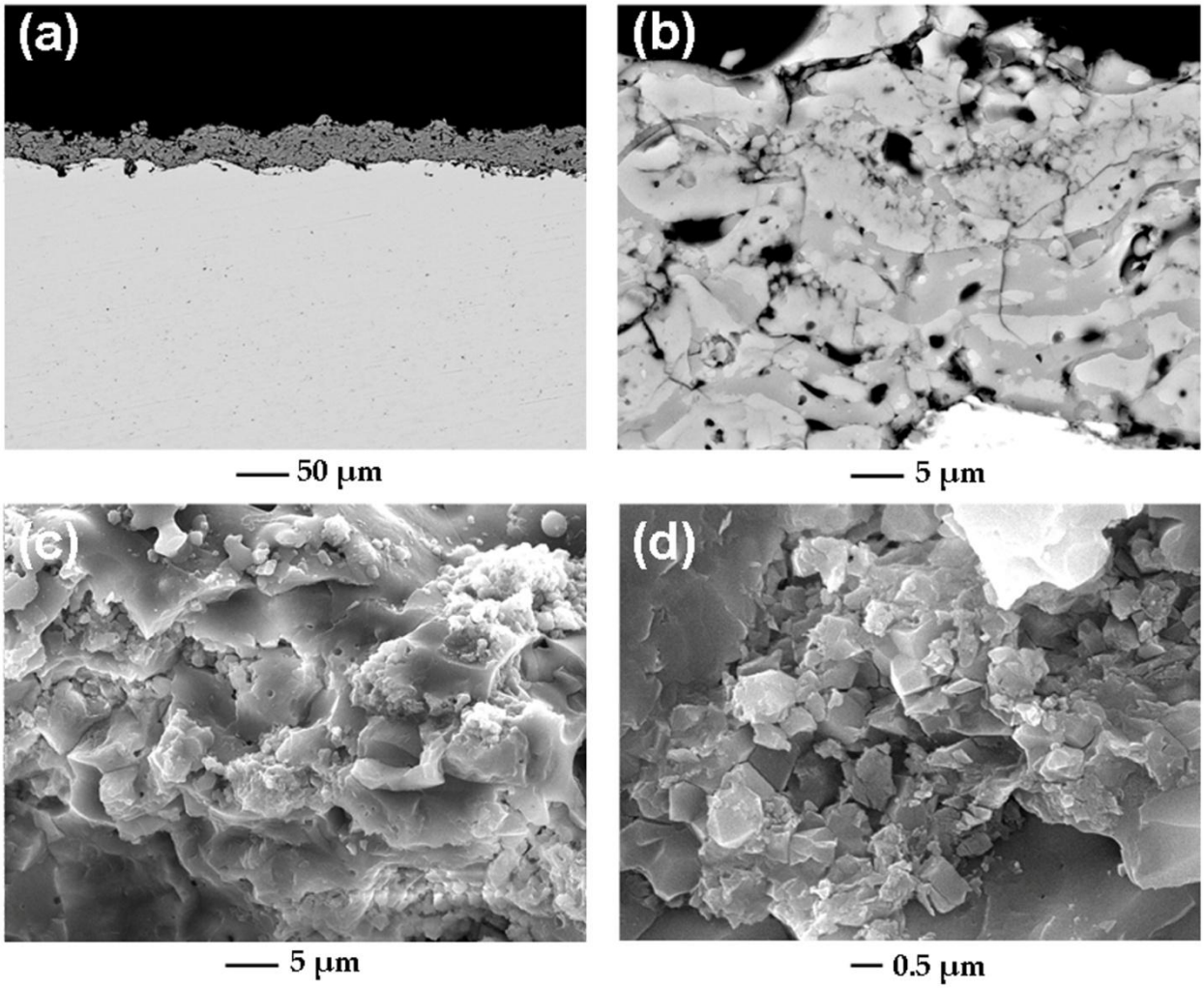

Figure 9

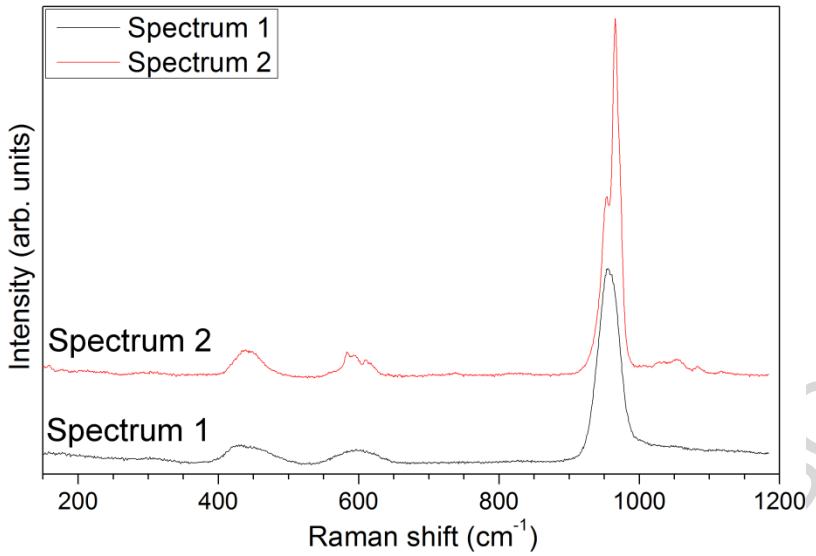

Figure 10

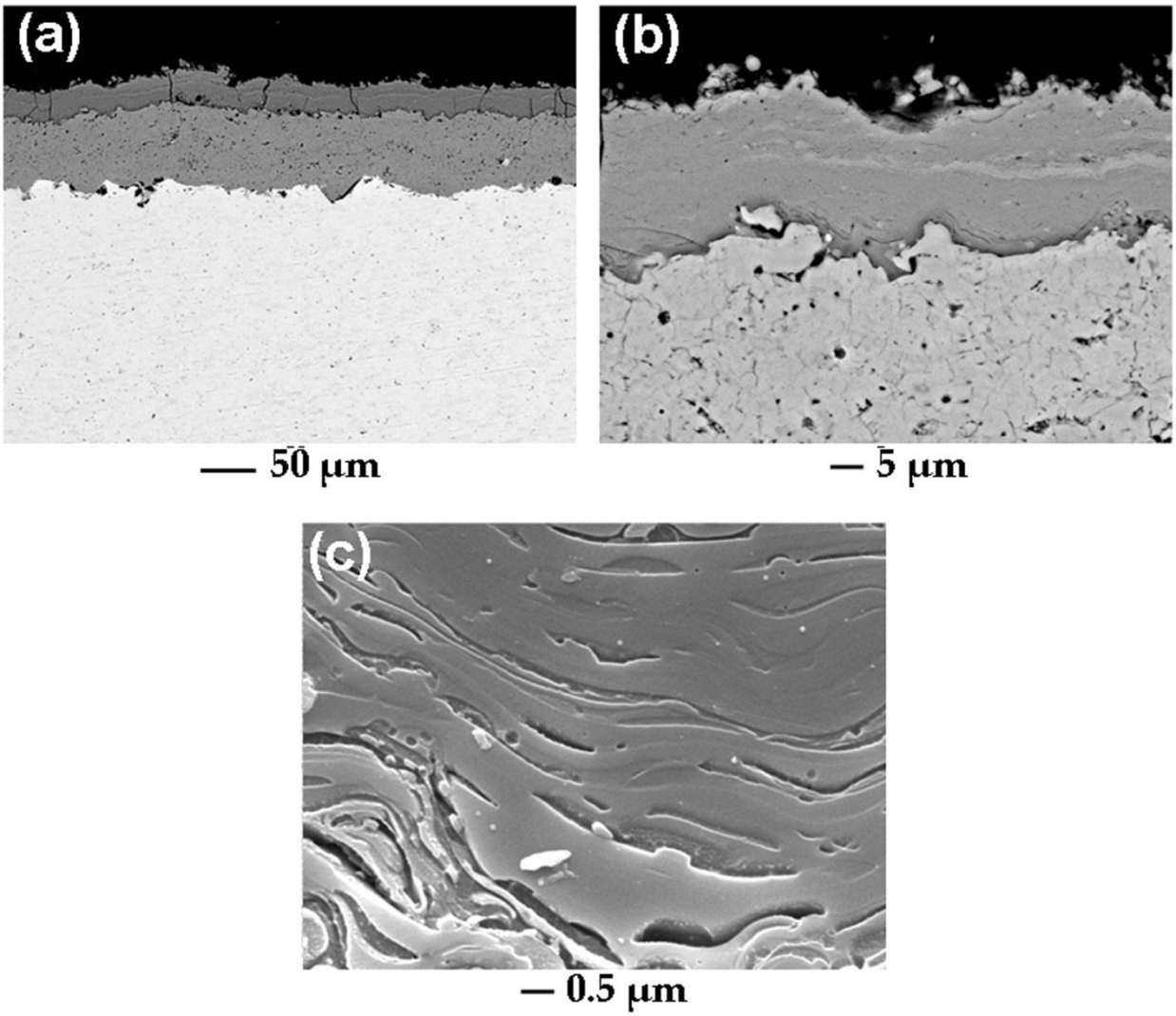

Figure 11

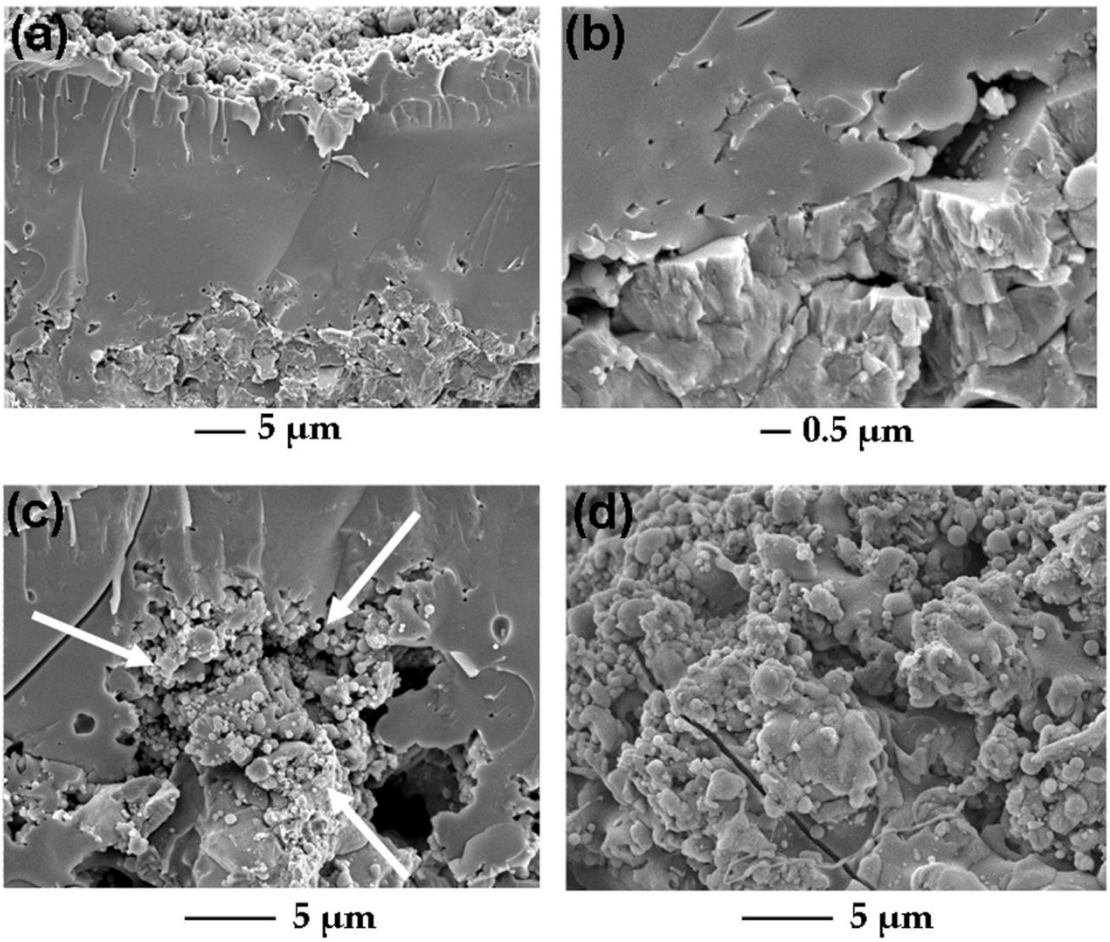

Figure 12

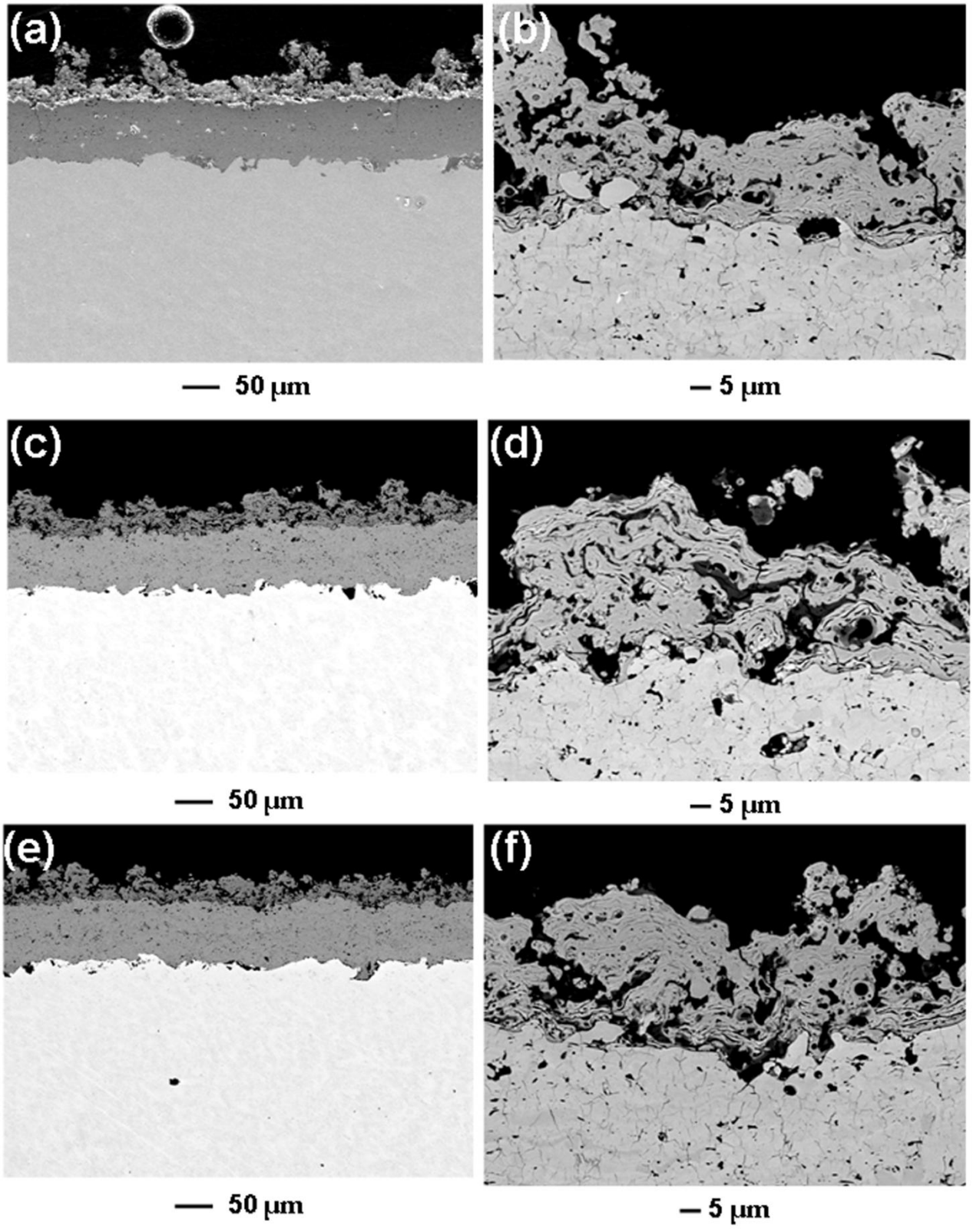

Figure 13

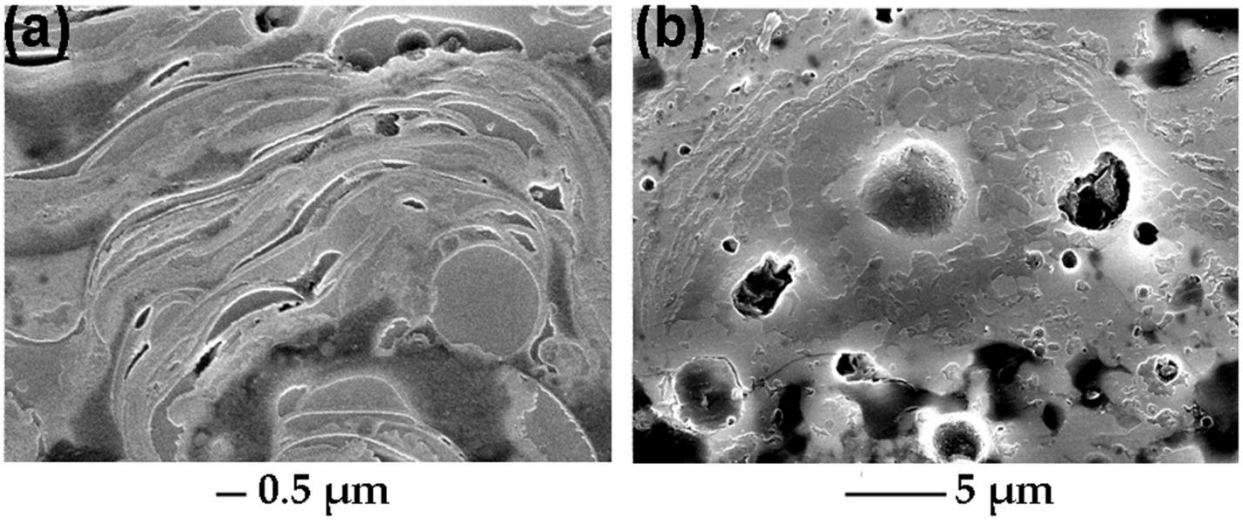

Figure 14

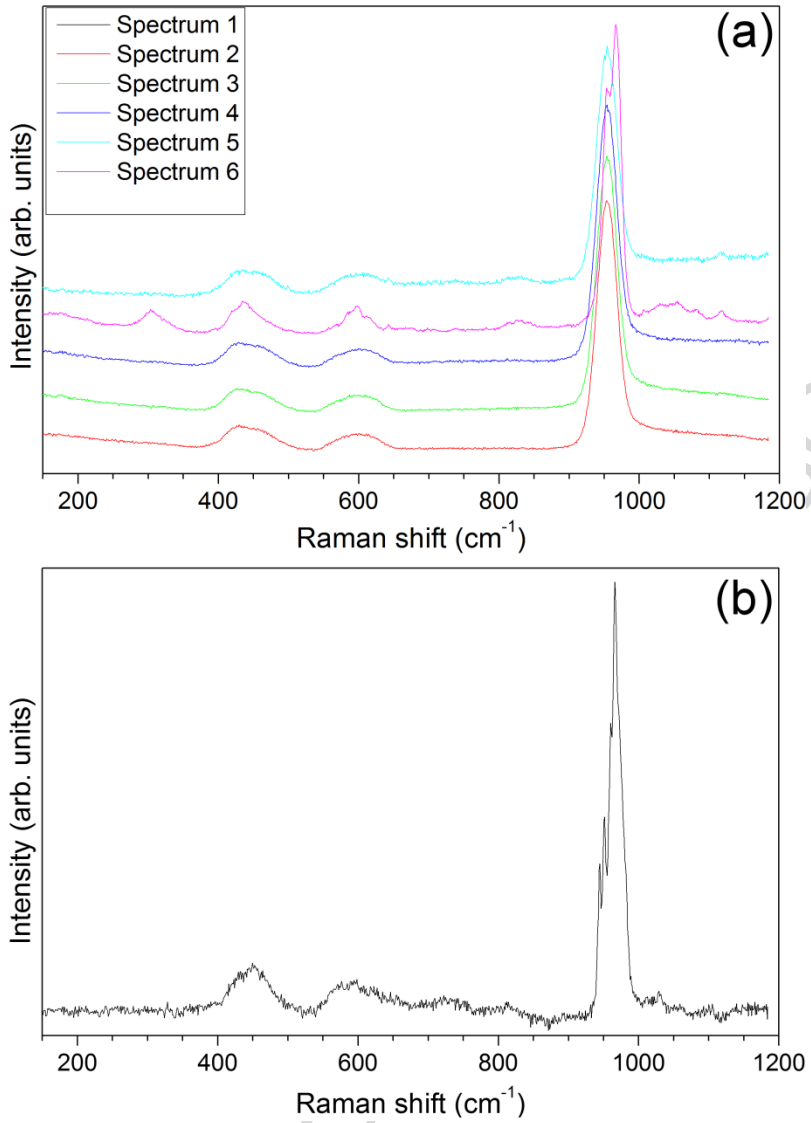

Figure 15

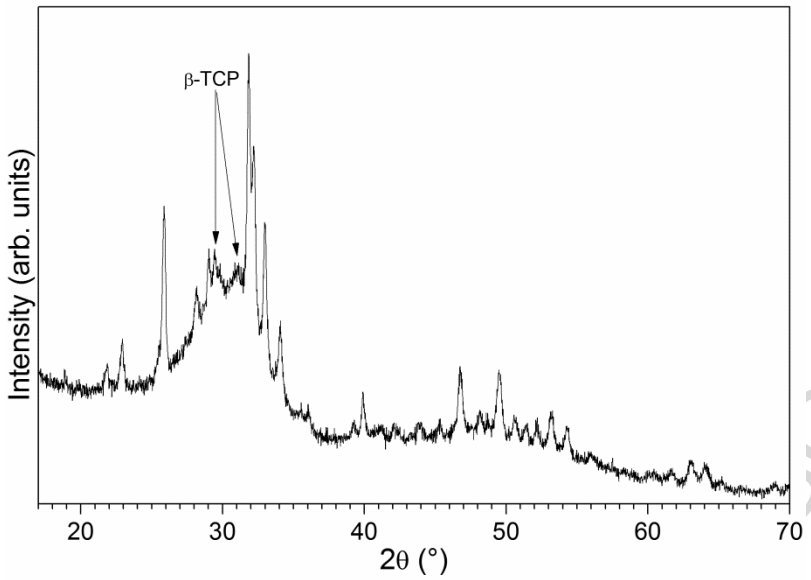

Figure 16

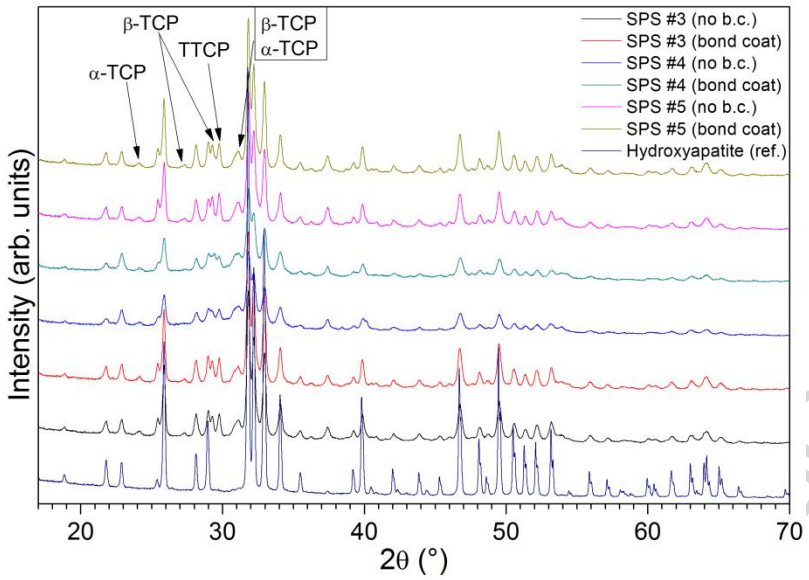

Figure 17

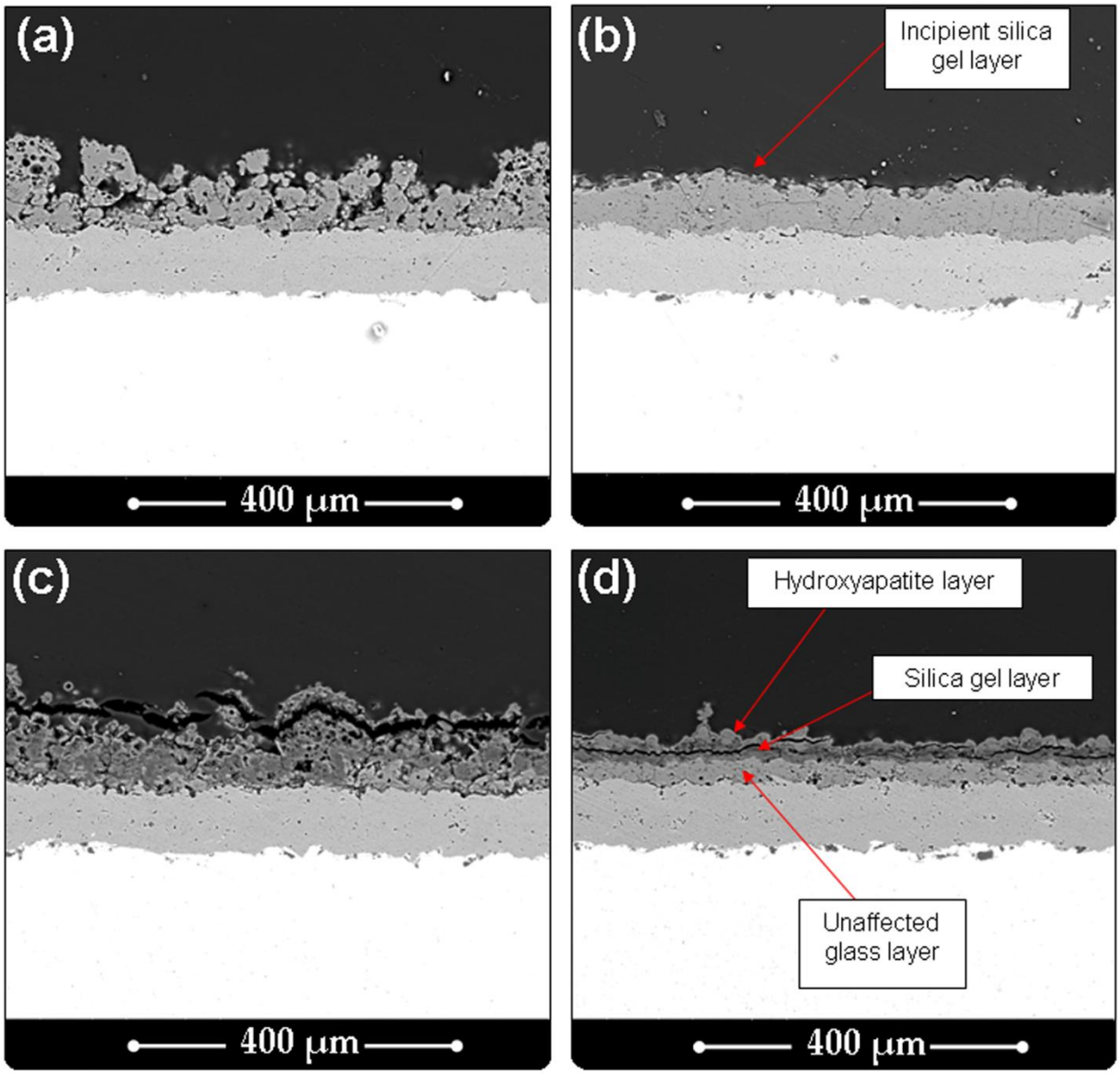

Figure 18

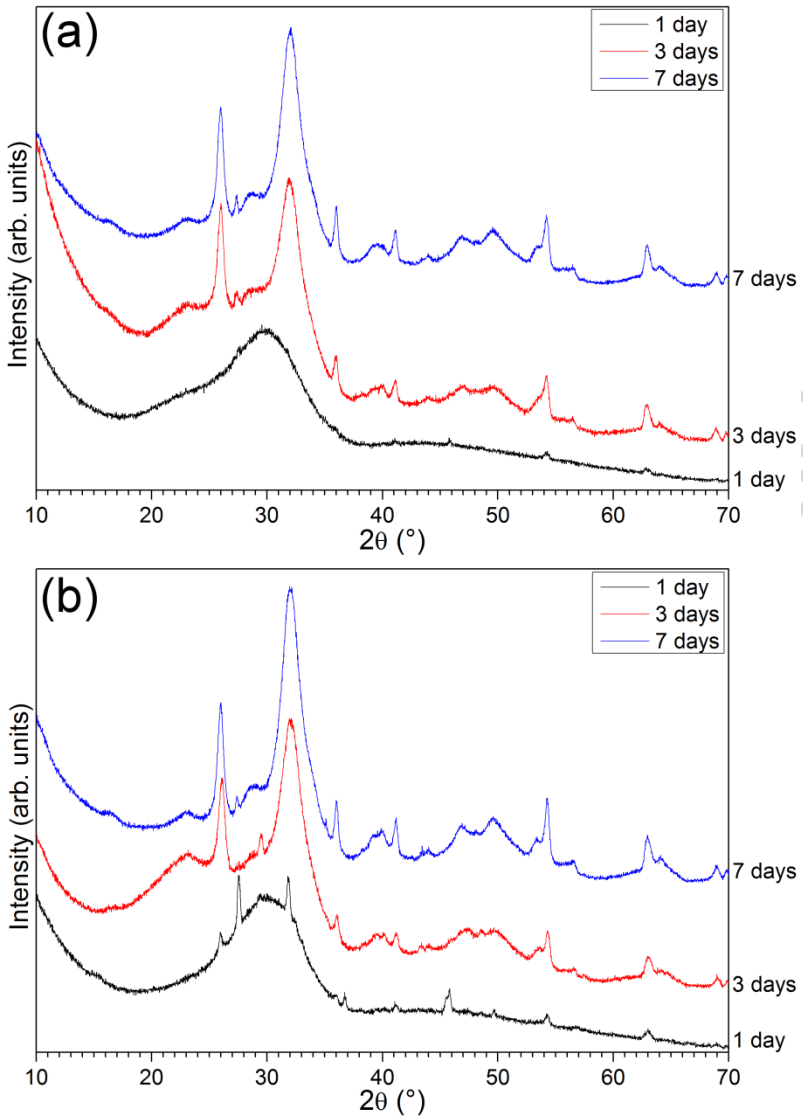

Figure 19

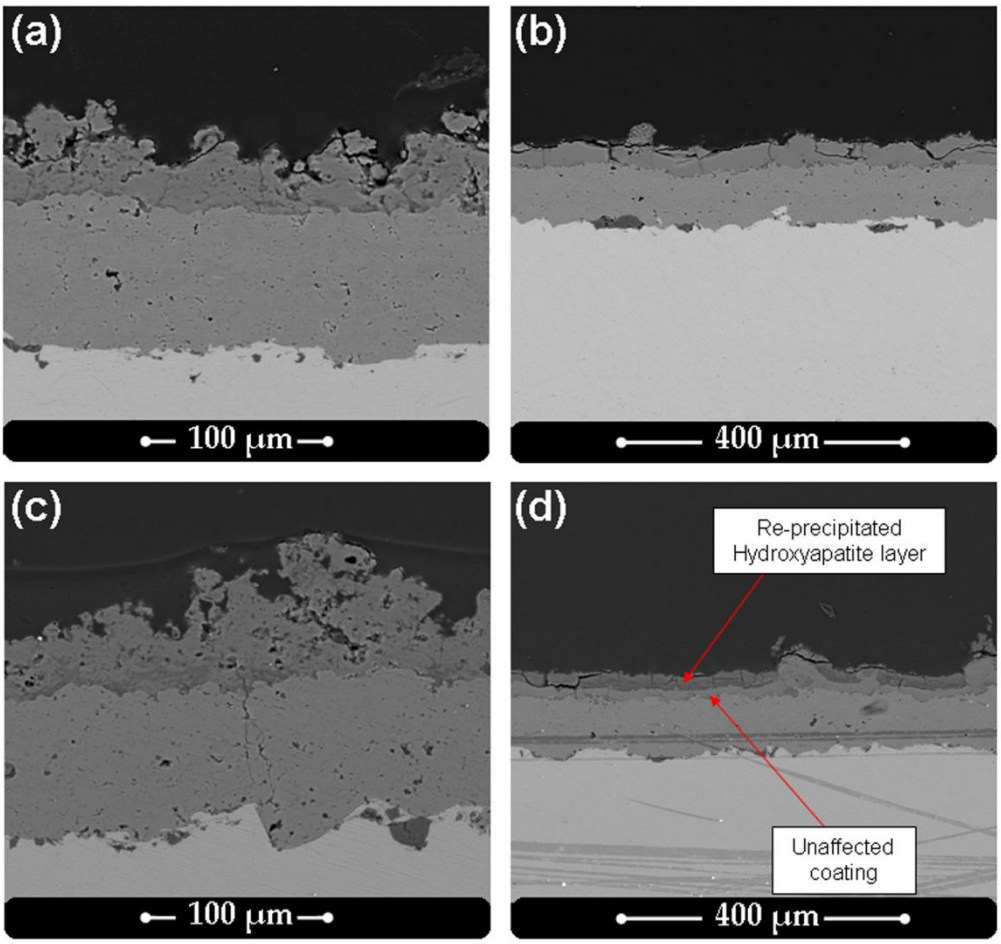

Figure 20

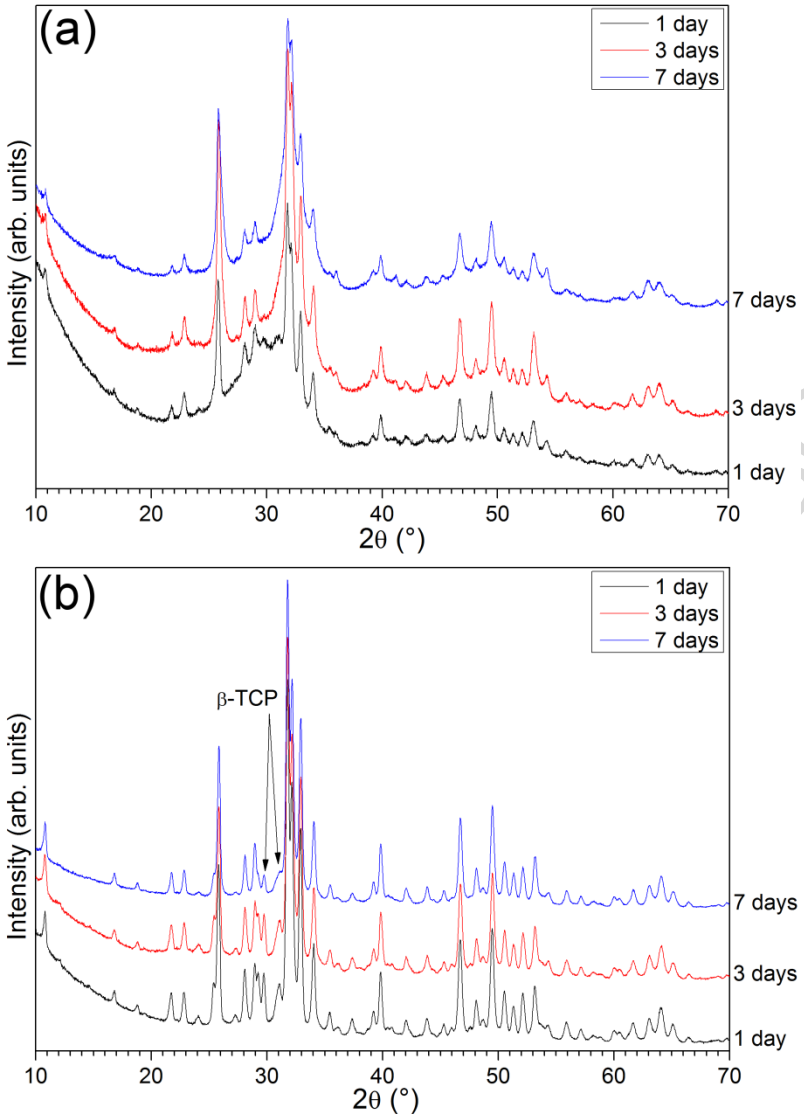

Figure 21

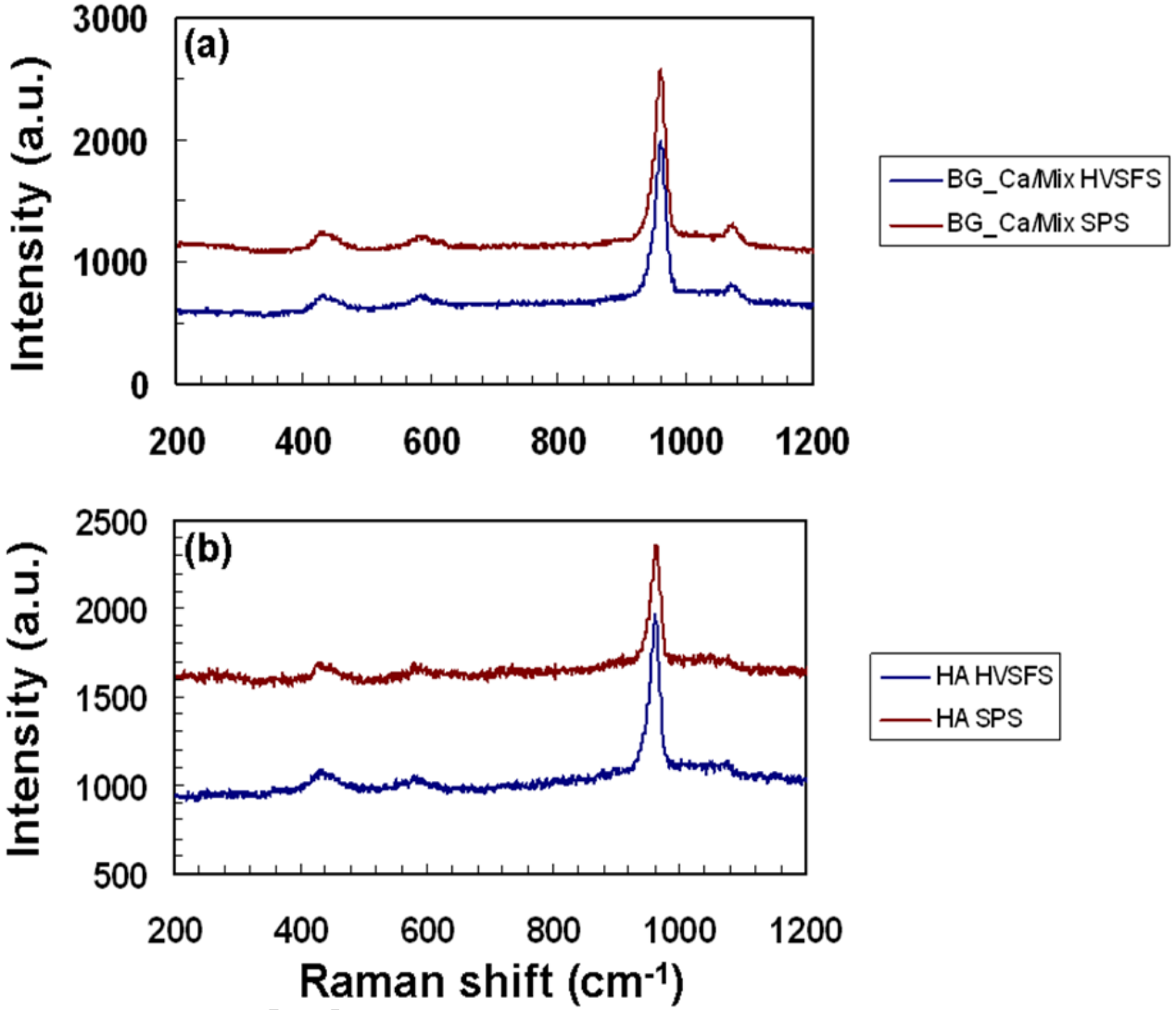

Figure 22

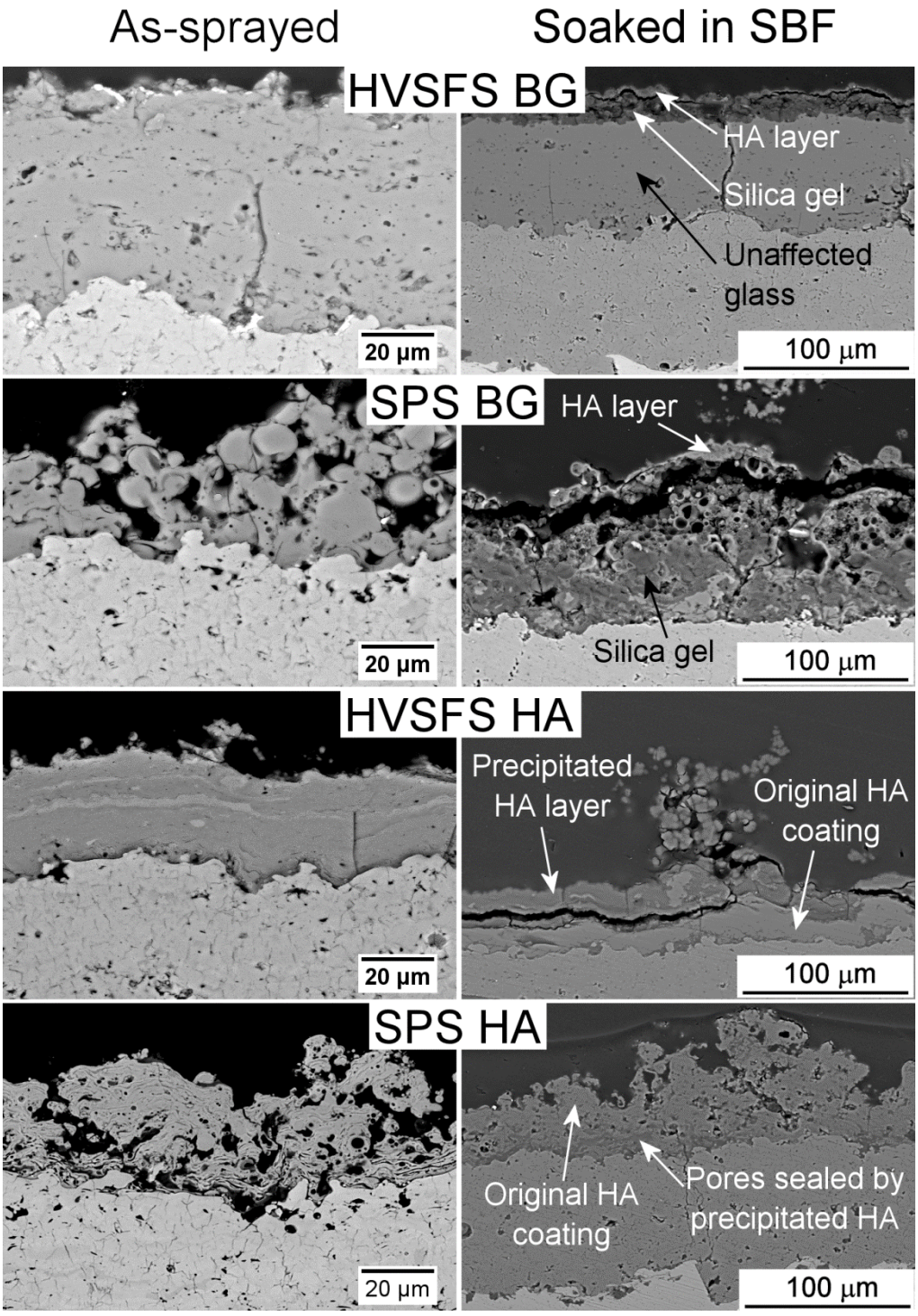

Graphical abstract

Highlights

Bioglass and hydroxyapatite layers deposited by SPS and HVSFS processes are compared

SPS coatings have porous columnar structure, with low particle flattening degrees

SPS bioglass layers are rapidly resorbable in simulated body fluid solution

HVSFS coatings are very dense, thin (<50 μm), with tightly bound, flattened lamellae

HVSFS bioglass layers react slower when immersed in simulated body fluid solution